Applied Materials Today 48 (2026) 103062

Contents lists available at ScienceDirect

Applied Materials Today

journal homepage: www.elsevier.com/locate/apmt

Revolutionary 3D-printed vertebral device with antibacterial silver-based nanocoatings for bone regeneration and antibacterial action

Gabriela Graziani [a,1,2], Daniele Ghezzi [a,b,2], Maria Sartori [c,*], Lucia Martini [c], Enrico Sassoni [d], Melania Maglio [c], Gianluca Giavaresi [c], Martina Cappelletti [b], Fabio Nudelman [e], Marco Boi [a], Matteo Montesissa [a], Nicola Baldini [a,f], Fraser Laidlaw [g], Donato Monopoli [h], Giuseppe Tedesco [i], Alessandro Gasbarrini [f,i], Milena Fini [j]

[a] Biomedical Sciences and Technologies and Nanobiotechnologies, IRCCS Istituto Ortopedico Rizzoli, Via di Barbiano 1/10, 40136, Bologna, Italy
[b] Department of Pharmacy and Biotechnology, University of Bologna, Via Irnerio 42, 40126, Bologna, Italy
[c] Surgical Sciences and Technologies, IRCCS Istituto Ortopedico Rizzoli, Via di Barbiano 1/10, 40136, Bologna, Italy
[d] Department of Civil, Chemical, Environmental and Materials Engineering, University of Bologna, Via Terracini 28, 40131, Bologna, Italy
[e] EaStCHEM School of Chemistry, The University of Edinburgh, David Brewster Road, Edinburgh EH9 3FJ, UK
[f] Department of Biomedical and Neuromotor Sciences, University of Bologna, Via Massarenti 9, 40128, Bologna, Italy
[g] School of Physics and Astronomy, University of Edinburgh, The King's Buildings, Peter Guthrie Tait Road, Edinburgh EH9 3FD, UK
[h] Department of Biomedical Engineering, Instituto Tecnológico de Canarias, Las Palmas de Gran Canaria, Gran Canaria, Spain
[i] Department of Spine Surgery, IRCCS Istituto Ortopedico Rizzoli, via G. C. Pupilli 1, 40136, Bologna, Italy
[j] Scientific Director, IRCCS Istituto Ortopedico Rizzoli, Via di Barbiano 1/10, 40136, Bologna, Italy

ARTICLE INFO

Keywords:
Spine surgery
Bone implants
Infection
MRSA
Silver
Ionized jet deposition
Custom-made prostheses
Orthopedics

ABSTRACT

Spinal orthopedic infections, with incidence rates of 15–20%, pose a significant challenge. To prevent this complication, metal-based antibacterial coatings are widely used. However, current coatings have several drawbacks, with possible toxicity or impaired osteointegration. This study aimed at evaluating the use of nanostructured silver-based coatings to provide antibacterial efficacy to 3D printed custom-made porous spine prostheses. Coatings were obtained by Ionized Jet Deposition, which guarantees nanostructuring and nanoscale thickness, both of which help avoid toxicity. To further mitigate interference with bone regeneration, the silver (Ag) was mixed with bone apatite (Bone). Deposition technique was also optimized for future industrial scale-up, and application to a real-scale prosthesis is demonstrated.

Our results showed that all the films were nanostructured and maintained the same composition as the target. The real-size device was effectively coated, also in the inner areas, potentially discouraging microbial contamination onto the entire device.

Ag and Ag-Bone films demonstrated remarkable *in vitro* efficacy against gram-positive and gram-negative bacteria, with no observed cytotoxicity. Both Ag and Ag-Bone apatite films showed significant bacterial inhibition activity also in an *in vivo* model infected with the Methicillin-Resistant *Staphylococcus aureus* USA 300 strain, demonstrating their promising future applications for tackling infection associated with spine devices.

1. Introduction

Vertebral body replacement is among the most challenging procedures in orthopaedic surgery, burdened by a 45.5 % complication rate, posing a huge societal, healthcare, and economic burden, which drives the research for innovative solutions [1–3].

Among its complications, spine infection, particularly after segmental resection, is critical, and may lead to a fatal evolution. Indeed, infection compromises the outcome, causing the need to restore stability and prevent spreading to the neighbouring visceral cavities [3–5]. Spine infection has high incidence rate, up to 15–20 %, varying depending on the underlying disease, the site, the surgical technique and, mostly, on

* Corresponding author.
E-mail address: maria.sartori@iot.it (M. Sartori).
[1] Present affiliation: San Raffaele Rome University, via di Val Canutta 247, Rome, IT.
[2] These authors contributed equally to the work.

https://doi.org/10.1016/j.apmt.2025.103062
Received 4 June 2025; Received in revised form 24 October 2025; Accepted 17 December 2025
Available online 26 December 2025

associated comorbidities, such as tumors, diabetes, or immunodeficient conditions [6–9]. The onset of infection correlates with impaired bone regeneration and mechanical instability, thus requiring additional surgery with a negative impact on the patient as well as on the healthcare system. The development of innovative solutions or clinical approaches should consider all these crucial aspects [10–18].

Orthopaedic implants, including spine prostheses, need to integrate successfully with bone tissue and this process requires the capability of implant surfaces to support adhesion, proliferation, and differentiation of the osteogenic cells. There are two approaches to achieve this: (i) tailoring the geometry and porosity of the device to promote bone ingrowth and mechanical interlocking, and (ii) functionalizing the implant surface by coatings with composition and surface morphology favourable to promoting the response of the host cells. Three dimensional -printed custom-made titanium implants, allow for the optimization of the macro- and micro- architecture, geometry, and mechanical properties of the device. This enhances stability and osteointegration while also allowing the therapeutic and surgical approaches to be tailored to the individual patient's needs and characteristics [19–23]. Indeed, they are being increasingly used in the spine, even for challenging applications such as column reconstruction after *en bloc* resection surgery for spinal tumours, giving promising results and positive clinical perspectives [24–27]. The implant surface finishing and the presence of nanostructured coatings also play key roles in the process of bone healing [28] in addition to the composition, crystallinity and surface morphology of the coating material, as they determine the availability of specific ions (such as *Ca*, P, Mg, Sr, Na, etc.) in the peri-implant environment [29].

Bone infection surrounding implanted devices is still an issue of concern [6,7] and when debridement, antibiotic therapy and implant retention (DAIR) is not sufficient, implant removal is mandatory. This circumstance is even more challenging in spine surgery, where the surgical options are limited by the need of avoiding damage to the noble structures and preserving mechanical alignment and stability [30]. Indeed, the presence of instrumentation (rods, plates, screws, cages, etc..) enhances by itself microbial colonization and exposes the patient to the risk of infection [31–33].

Infection arises from bacterial colonization of the implant surface, on which microorganisms proliferate and produce a biofilm, a complex structure composed of an extracellular matrix that protects bacteria from the host immune system and from antibiotics, allowing colonization of other sites [34–36]. Controlled antibiotic release systems such as antibiotic impregnated devices or antibiotic loaded coatings can be a promising alternative, as they allow to deliver higher concentrations of antibiotics directly in the infection site, thus enhancing efficacy and lowering systemic toxicity. However, the incidence of bacterial strains resistant to several antibiotics is an increasingly serious issue in medicine, and also derives from the frequent use of these antibiotics for impregnating implantable medical devices such as central venous catheters [37] and is clearly testified by the enormous discrepancy between the increase in hospital visits and that of infections contracted during the visits (for example, +8 % *vs* +62 %, respectively, from 1999 to 2005) [38]. Metal-based coatings, and in particular, silver coatings, which are widespread on the market, have shown the ability to inhibit bacterial adhesion and biofilm formation, showing high efficacy against both gram-negative and gram-positive bacterial strains [39,40]. However, traditional coatings exhibit some drawbacks, due to insufficient control over metal release, leading to toxicity as well as to excessive thickness, causing cracking and detachments, and, in turn, scarce control over antibacterial efficacy [41]. More advanced deposition techniques, such as magnetron sputtering, permit a better control over film characteristics and a fine rune of ion release, but pre-conditioning of the substrate and/or post deposition treatments are normally needed [42].

Our preliminary data have shown that silver-based nanostructured coatings deposited by Ionized Jet Deposition (IJD) exhibit significant inhibition of bacterial growth *in vitro* without causing cytotoxicity and/or nanotoxicity both *in vitro* and *in vivo* [43], but their antibacterial efficacy has never been tested *in vivo*. In addition, applicability of IJD and plasma-assisted techniques in general is limited by the fact that they are regarded as line-of-sight techniques, and are subjected to the so-called shadowing phenomenon, *i.e.* the parts that are not directly exposed to the plasma plume remain uncoated. For this reason, the combination of nanostructured coatings by plasma-assisted techniques and 3D printed scaffolds has not been explored. In addition, this approach would permit to have multi-scale featured in the implants starting from the nanoscale (providing antibacterial efficacy and optimal adhesion to the substrate), but also encompassing micro- and macro- scales, where geometry and shape of the implants is customized to boost integration and to be patient-specific.

The use of nanostructured silver as coating, is still the subject of debate. Nanostructuring offers great advantages to the process of implants osseointegration [44–45], but, controversial data and concerns have been raised about the potential toxicity to biological systems due to the dimensional issue [46]. Silver exerts multiple antimicrobial mechanisms, including interaction with microbial membranes, leading to structural damage and increased permeability, disruption of cellular respiration and ATP production by interfering with essential enzymes in the electron transport chain, DNA damage, protein impairment, and generation of reactive oxygen species (ROS) [47,48]. However, the same mechanisms can adversely affect mammalian cells. Excessive ROS production induced by silver may overwhelm the cellular antioxidant defence system, leading to oxidative stress, mitochondrial dysfunction, lipid peroxidation, DNA damage, and ultimately apoptosis or necrosis [49]. Hence, investigating its potential toxicity is of paramount importance. To promote osseointegration, calcium phosphates, and, ion particular, hydroxyapatite coatings are widely used, and represent, to date, the most explored clinical option [29]. In particular, our previous results have shown that, thanks to their biomimetic composition and multiscale (micro- to nano-) morphology, bone apatite coatings obtained by IJD can guide cellular behaviour and promote differentiation towards the osteogenic lineage [28,43], thus appearing as a promising strategy to oppose possible detrimental effects of metals on host cells. Among different calcium phosphates, and, in particular compared to stoichiometric apatite IJD coatings of biogenic hydroxyapatite has shown a better behaviour in terms of durability and capability to promote host cells behaviour [50,51].

Merging the antibacterial capacity of silver, with and without the use of bone apatite to reduce potential toxicity, the aim of this study was to create a new nanostructured antibacterial and osseointegrative coating that can be effectively combined with a custom-made spine prosthesis to obtain absence of toxicity to host cells combined with antibacterial activity. To further promote the enhancement of bone regeneration and integration, we investigated a combination of silver and bone apatite, in view of their clinical application. Silver-bone apatite coatings are designed with a gradient in composition, with a higher amount of silver in the surface, progressively reducing in depth, so as to achieve a higher release of silver in the first hours after implantation (when infection is more probable) and then an increasing release of bioactive ions to boost regeneration in the later stages. We showed that the coatings can be applied to porous-custom made prostheses without significant shadowing or loss of efficacy. The developed approach was evaluated *in vitro*, and *in vivo*, also targeting the methicillin-resistant *Staphylococcus aureus* (MRSA) USA 300 strain, which is scarcely susceptible to several antimicrobial compounds currently used in clinics [52].

2. Materials and methods

2.1. Design and additive manufacturing of samples for in vitro and in vivo test

Starting from previous experience in the reconstructions of segmental defects [53], Instituto Tecnológico de Canarias (ITC)

exploited the gyroid-type structures deformed in the load direction. Three-dimension printed scaffolds for all *in vitro* and *in vivo* preclinical investigations were manufactured using EBM process (ARCAM S12) with Ti6Al4V powder layers of 50 μm, beam current of 44 mA, voltage of 60 kV and electron beam size of 200 μm in a vacuum condition (10−3 mbar) controlled by using helium. A constant temperature of 700 °C was maintained inside the vacuum chamber throughout the building. Titanium alloy was used as raw material, with an average particle diameter of 50 μm. No heat treatment or other post processing steps were applied. Ti6Al4V has been selected as the most widely used material for orthopaedic prostheses in general, and porous Ti6Al4V is the gold standard for custom-made spine prostheses following vertebral resections, where the high and multi-axial loads prevent the possibility to use ceramics or polymers.

For the physical-chemical investigations of the coatings, and the *in vitro* biological investigations (antibacterial efficacy and bioactivity), and the *in vivo* studies, porous disks AM with a height of 5 mm and a diameter of 4, 5 and 10 mm were manufactured, all maintaining the pore size of the large-scale prostheses. Because of challenges posed by characterization of highly rough and highly porous substrates and/or by the interference of metallic substrate with the characterization of coatings, reference substrates (*i.e.* glass wafer for XRD, and flat Ti6Al4V disks for pre-screening of coatings morphology and homogeneity and for absence of cytotoxicity of Ag-Bone films) were also used.

2.2. Materials

For manufacturing the coatings, silver targets were purchased from Kurt J. Lesker, PA, USA and used as supplied. Bone apatite targets were obtained as described in a previous paper [54]: bovine cortical shafts were deproteinized for 14 days in NaOCl 2 wt % for complete removal of organic fractions. Ag and Ag-bone films were deposited onto 3D printed porous titanium substrates, supplied by Instituto Tecnológico de Canarias - ICT in different sizes (as specified in Supplementary File Table 1). Glass wafers and flat titanium disks were also used as reference substrates.

2.3. Composite targets manufacturing and coatings deposition

Coatings were obtained by silver (Ag) and silver-bone apatite (Ag-Bone) composite targets (Fig. 1). To obtain the latter, different techniques were tested, including impregnation in Ag-salts and deposition of silver on bone apatite and *vice versa*. The optimal target preparation route was selected based on the homogeneity of the coatings and the inhibition of planktonic growth of *Escherichia coli* (*data not reported*).

Briefly, bone apatite was deposited onto silver films by IJD to create a bone apatite film onto the top of the silver target. Upon progressive ablation, both materials were deposited on the surface of the prostheses, with an increasing concentration of bone apatite for increasing depth. This was selected to permit to have a higher release of silver in the first hours (when infection is more frequent) and higher release of bone apatite in the later timepoints, where osseointegration is needed. To obtain the composite targets, bone apatite was deposited for 1 hour onto silver target to obtain a film thickness of about 2 μm. This was selected based on a pre-screening of different deposition times, based on coatings homogeneity and antibacterial efficacy (data not reported). For this step, deposition conditions were based on a previously published method [54]. Working voltage and electron beam frequency were set at 17 kV and 7 Hz, while target-substrate distance was 8 cm.

Once the targets were prepared, both silver and silver-bone apatite targets were deposited for 60 min, using the same conditions. The whole target preparation and coatings deposition and conditions are schematized in Fig. 1. IJD is a versatile technique where the characteristics of the coatings, including their thickness and surface roughness can be determined by deposition parameters and in particular by deposition time, which directly correlates with film thickness. Here, deposition parameters were selected based on previous results for silver and bone apatite films: target to substrate distance 8 cm, frequency 7 Hz, 22 kV voltage. The substrate was kept rotating while the target was fixed. For all samples, deposition was carried out in two steps, along two opposite directions, to coat all areas of the samples. Each deposition was carried out for 60 min, as specified above. No pre- or post- deposition treatments were performed, to reduce manufacturing time and increase industrial scalability. Indeed, high adhesion also in the absence of these treatments is one of the main advantages of IJD compared to similar techniques, such as magnetron sputtering [55].

2.4. Preliminary assessment of the properties of ag-bone films in comparison with ag-films

Films composition was first studied by X-ray Diffraction (XRD), performed on reference substrates (glass slides), to avoid interference of the metallic substrate with the coatings' spectra. XRD was carried out using a Malvern PANalytical Empyrean series III instrument (40 kVand 30 mA, 2θ range=20–80, step size=0.01, time per step=30 s).

Since Ag-Bone samples had never been previously developed, a preliminary characterization was performed to investigate their characteristics prior to deposition on the final porous implants. To this aim morphological and compositional characteristics of the coatings and their homogeneity were first tested on non-porous titanium alloys disks. This was done by using a Field Emission Gun Scanning Electron Microscopy (FEG-SEM, Tescan Mira3, CZ, working distance = 10 mm, voltage = 10 kV), and Energy Dispersive X-ray Spectroscopy (EDS) maps. A working voltage of 10 kV was used for Scanning Electron Microscopy (SEM) and EDS. The samples were made conductive before observation by coating them with carbon. Uniformity of the coatings and absence of defects were verified by examining 3 areas on two different samples and observing the eventual presence of defects (such as uncoated areas, cracks or delamination). EDS, was performed to study homogeneity in distribution of Ag, P and *Ca*, using a Bruker probe coupled with a field emission gun scanning electron microscope.

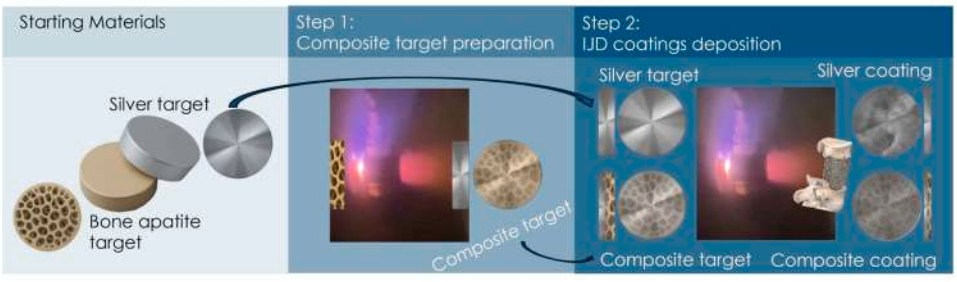

Fig. 1. Materials, composite targets preparation and final coatings combinations.

2.5. Compositional and morphological characterization of the coatings on vertebral prostheses

Following the deposition of the films on Ti_6Al_4V alloy porous samples, EDS and Inductively Coupled Plasma Optical Emission Spectroscopy (ICP-OES) were performed to detect their elemental composition. ICP-OES was performed using a ICP-OES Perkin Elmer Optima 8300, equipped with a Cross flow nebulizer and nebulization chamber Scott. RF 1500 W, Plasma Ar 12 l/min, after digesting the samples in 1 ml acetic acid for 24 h. EDS was performed as described above (cfr. §2.4). In addition, EDS maps for silver and, when relevant, calcium and phosphorous, were obtained to study coatings homogeneity.

FEG-SEM was performed on the porous samples to detect possible alterations to the substrate porosity or pore shape. Absence of defects was also verified as described for non-porous samples.

The thickness of the Ag and Ag-Bone layers, as well as their homogeneities and the possible presence of interlayers were investigated by Focus Ion Beam-Scanning Electron Microscopy (FIB-SEM) using a Zeiss Crossbeam 550 equipped with an inlens, secondary electrons and backscattered electrons detectors and an Oxford Instruments X-Max^N 150 energy-dispersive X-ray spectroscopy (EDS) detector. Milling was done at an ion beam accelerating voltage of 30 kV and beam current 300 pA, while SEM imaging was performed with an accelerating voltage of 1.5 kV. FIB-SEM analysis was coupled with EDS measurements, carried out with an accelerating voltage of 10 kV. Prior to milling, a protective layer of carbon several μm thick was deposited over the region of interest using the Gas Injection System.

Silver release was measured by immersing the samples in 1 ml PBS and store them in incubator, mimicking the protocol followed by cells tests. At different timepoints (3 h, 1 day, 7 days), silver amount was quantified by ICP-OES to match silver concentration with biological results.

Durability of the films was assessed at day 7 (corresponding to the length of animal tests and the target duration of the coatings), following immersion in PBS, by performing FEG-SEM (secondary and backscattered electrons) and EDS maps on the samples to detect and quantify residual presence of the coatings.

2.6. Optimization of the deposition on a real scale vertebral prosthesis

Because IJD is a plasma assisted technique, it could be subjected to shadowing, when applied to objects having pores and/or large dimensions.

For this reason, special attention was devoted to: (i) assessing absence of alterations to substrates porosity, pore size morphology and surface finishing; (ii) studying the uniformity of coating of complex substrates when moving further from the plasma plume and inside the porosity.

For the latter, two different conditions were tested for obtaining the best substrate coverage, differing for the angle between the prosthesis and the plasma plume, that influences the ability of the plasma plume to enter the prosthesis and, consequently, the extent of the shadowing effect. To this aim, both 0° (deposition onto the cylinders bases) and 90° (deposition onto the cylinders longitudinal surfaces) deposition were carried out. These angles were selected as they are the two most different positions in which the samples can be position in IJD deposition.

For the analysis, an entire vertebral prosthesis was 3D printed on 6 separate disks with the aforementioned dimensions (height of 5 mm and 10 mm in diameter). The disks were connected and composed in the shape of the vertebra for the deposition, then divided for SEM observations. Thus, it was possible to study the presence/absence of the coating, as well as its morphological characteristics, at different depths in the substrate and both at the surface of the prosthesis and in its center.

2.7. Biological investigations

2.7.1. Antibacterial efficacy in vitro

Optimal films for *in vivo* testing were selected based on pre-screening aimed at assessing their antibacterial efficacy *in vitro*. The antibacterial activity of the coated disks/cylinders was assessed testing standard reference pathogenic strains commonly used in ISO protocols, specifically *E. coli* ATCC 8739, *Staphylococcus aureus* ATCC 6538P In addition, the methicillin-resistant *Staphylococcus aureus* (MRSA) USA300 strain was included due to its clinical relevance; since its emergence in the early 1990s, *S. aureus* USA300 has rapidly disseminated and has become a leading cause of community-associated and hospital-acquired infections, particularly skin and soft tissue infections among otherwise healthy individuals [56,57]. All cultures were prepared by inoculating a single bacterial colony (pre-grown on Tryptic Soy Agar (TSA) plates for 18–20 h) in 50-mL tubes with 5 mL of Tryptic Soy Broth (TSB) medium. Cultures were grown overnight at 37 °C under agitation and then diluted based on standardized optical density measurements at 600 nm (OD_{600}) to achieve a final concentration of approximately 10^6 CFU (Colony Forming Units) mL^{-1}. For the test, the control (titanium substrate without coating) and the coated samples were placed at the bottom of 48-wells microplates that were filled with 500 μL bacterial suspension to be further incubated for 8 h at 37 °C under shaking conditions (130 rpm). At the end of the incubation, the growth of the microorganisms was assessed by spreading serial dilutions of cultures on TSA plates and by counting the number of CFU mL^{-1} after 18–24 h of incubation at 37 °C. Triplicates were performed for each experimental condition.

2.7.2. Cell cultures

For *in vitro* cytotoxicity tests, MG63 osteoblast-like cells were used. Cell culture medium was prepared using Dulbecco's modified Eagle's medium (DMEM, Sigma, lot SLBz1832) additioned with 10 % fetal bovine serum-FBS (Euroclone, lot EUS028877), and 100 IU/ml penicillin - 100 μg/ml streptomycin (Sigma, lot 128M4809V). MG63 cells preserved in −180 °C liquid nitrogen were thawed for the test and cells were incubated in a 75 ml flask in DMEM at 37 °C in 5 %CO2 humidified atmosphere. Upon reaching 80 % confluence, cells were treated with trypsin 0.05 % (w/v)/EDTA 0.02 % (w/v) (Sigma, lot SLCC0835) for cell release and counted in a Neubauer chamber using Erythrosin B exclusion dye (Thermo Fisher, Kandel, Germany) prior to use.

For the *in vitro* bioactivity study, primary normal human osteoblast (nHOb) cells (Lonza LOCC2538) (P2 upon arrival) were expanded under standard culture conditions and used at passage 4 (P4) for all experiments. Cells were cultured using the provided culture medium OBM™ (Osteoblast Growth and Differentiation Basal Medium (LONZA) supplemented with 10 % FBS, 100 U/ml penicillin, and 100 μg/ml streptomycin), under standard conditions. Upon reaching 80 % confluence, nHOb were treated with trypsin 0.05 % (w/v)/EDTA 0.02 % (w/v) (Sigma, lot SLCC0835) for cell release and counted in a Neubauer chamber using Erythrosin B exclusion dye (Thermo Fisher, Kandel, Germany) prior to seeding in contact with materials.

2.7.3. In vitro cytotoxicity evaluation of silver and bone apatite/silver nanostructured coatings

In vitro cytotoxicity tests assessed the biological safety of silver and of the new combined bone apatite/silver coatings, according to the guidelines provided by the UNI EN ISO 10,993 –Biological evaluation of medical devices - Part 5 (2009): Tests for *in vitro* cytotoxicity. Specific biological parameters were evaluated after the direct interaction of the coatings with MG63 osteoblast-like cells. These screening tests were performed by depositing silver (**Ag**) and silver/bone apatite (**Ag-Bone**) coatings onto flat Ti_6Al_4V disks (height of 5 mm and diameter of 10 mm) in comparison to uncoated substrate (**Ti-substrate**). All materials were sterilized by gamma rays at a dose of 25 kGy before biological tests.

Each material was placed into a six-well plate and MG63 cells suspension at a concentration of 2.0×10^4 cells/cm^2 was seeded onto and

around the experimental and control materials ($n = 6$), while cells seeded in six wells with DMEM only and with 1 % phenol solution in DMEM were used as negative and positive controls, respectively. Plates were incubated at 37 °C in 5 % CO2 atmosphere for 72 h. After 72 h of culture, the amount of lactate dehydrogenase (LDH) enzyme released into the culture medium was measured adopting the LDH kit (Roche lot 11,644,793,001), according to manufacturer instructions. Briefly, after incubation of cells supernatants with the reaction mix, the colorimetric reaction proportional to the amount of enzyme in culture supernatant was measured with a spectrophotometer at 490/655 nm (Micro Plate reader – Bio-Rad Laboratories, *CA*) and the values expressed in percentage of cytotoxicity by applying the following formula:

$$\%\ Cytotoxicity = \frac{(\mathrm{LDH})\ experimental\ coating\ -(\mathrm{LDH})\ negative\ ctr}{(\mathrm{LDH})\ positive\ ctr\ -(\mathrm{LDH})\ negative\ ctr}$$

Cell proliferation was evaluated using the WST-1 test (Roche, lot 38,418,000), which represents a sensitive method to perform a quantitative evaluation of cell proliferation, by measuring the amount of dye generated by a specific enzyme and directly proportional to the number of living cells. Briefly, WST1 reagent was added to a fresh culture medium in a final concentration of 1:10 and after 4 h of incubation the final dye produced by viable cells was quantified by measuring the absorbance at 450/625 nm. Results are reported as optical density (OD) and values directly correlate with cell number.

Finally, a solution of neutral red at 0.033 % (Sigma, lot SLBW7291) warmed to 37 °C, was added to all wells at the end of the experimental times for further 90 min to evaluate the morphology of the cells around the coatings and to additionally quantify the viability of cells by means the solubilization of the vital dye. The absorbance of solubilized dye was measured by spectrophotometer at 540 nm. Data are reported as percentage of viability onto negative control.

2.7.4. *In vitro bioactivity study on the combined bone apatite/silver nanostructured coating*

An *in vitro* bioactivity study was conducted to investigate the osteogenic potential of the combined Ag/Bone coating. Normal human osteoblasts (nHOb) were seeded at a density of 5×10^4 cells/ml onto silver/bone apatite coated porous customized substrates (5 mm height, 10 mm in diameter) and onto a control substrate without any coatings manufactured by ITC. After cell seeding, cultures were maintained in OBM™ basal medium for 24 h to allow initial cell adhesion and proliferation. On day 2, the medium was replaced with osteogenic differentiation medium consisting of basal medium with the addition of supplements and growth factors (OGM™ Differentiation SingleQuot) which was used for the remainder of the experimental period. As for all biological tests (cytotoxicity and antibacterial investigations) all substrates were sterilized by gamma rays at a dose of 25 kGy. The osteoblasts were also directly seeded onto tissue culture polystyrene, used as a standardized 2D culture control (CTR).

At each experimental time, 3, 7, 14 days, cell metabolic activity was tested with Alamar Blue (Serotec, Oxford, UK). The reagent, added to the experimental and control substrate (1:10 v/v) and incubated for 4 h at 37 °C, incorporates a fluorometric growth indicator related to the detection of metabolic activity. The fluorescence was read at 530ex-590em nm wavelengths using a Micro Plate reader (VICTOR X2030, Perkin Elmer, Milan, Italy) and although fluorescence values were not normalized to cell number or surface area, all experiments were performed using equal seeding densities and reagent volumes to ensure consistency across conditions. The fluorescence values were expressed as relative fluorescence units (RFU).

Cell supernatants were collected from each condition, centrifuged to remove particulate matter and tested with enzyme-linked immunosorbent assays (ELISA) to quantify the release of some of the major osteogenic marker and inflammatory cytokines even elicited by the silver presence. Briefly, 100 µL of cell culture supernatant was added to 96-well plates coated with antibodies specific to human alkaline phosphatase (ALP - Cloud-Clone Corp, Katy, TX, catalog number: SEB472Hu), Type I collagen (COL1 - Cloud-Clone Corp, Katy, TX, catalog number: SEA571HU) osteocalcin (OC – Raybiotech life, Inc, Parkway Lane Suite, GA, US, catalog number: ELH—Osteocalcin), osteoprotegerin (Human TNFRSF11B/OPG - Booster Biological Technology, Pleasanton, *CA*, US, catalog number: EK0480), RANKL ligand (TNFS11/RANKL – Booster Biological Technology, Pleasanton, *CA*, US, catalog number: EK0842), interleukin 6 (IL-6–4A Biotech Co. Ltd, Suzhou, CN, catalog number: CHE0009), and caspase 3 (CASPASE 3-Booster Biological Technology, Pleasanton, *CA*, US, catalog number: EK1425). Each assay was performed according to manufacturer's instructions and the concentration of each marker was calculated by reading the absorbance at 450 nm on a spectrophotometer (MicroPlate reader, Bio-Rad Laboratories, Hercules, *CA*, USA) and referring to a standard curve of antigen concentration.

At 7 and 14 days of culture, total RNA was extracted from nHOb seeded directly onto Ag-Bone and Ti-substrate as well as from nHOb seeded onto polystyrene well (used as control to verify regular cell proliferation, differentiation and gene expression, regardless of substrate presence), using Trizol® reagent (AMBION by Life Technologies, Carlsbad, *CA*, USA) and Chloroform (Sigma Aldrich) until harvesting the aqueous phase. The procedure was continued by using the commercial PureLinkTM RNeasy Mini Kit (AMBION), quantified by NANODROP spectrophotometer (NANODROP 2720, Thermal Cycler, Applied Biosystem) and reverse transcribed with SuperScriptVILO cDNA Synthesis Kit (Life Technologies), following the manufacturer's instructions. The obtained cDNA was diluted to the final concentration of 5 ng/µL for each sample, taking into account the starting amount of RNA, to exploit the same range of amplification efficiency. Semi-quantitative polymerase chain reaction (PCR) analysis was performed for each sample, in duplicate, in LightCycler 2.0 Instrument (Roche Diagnostics GmbH, Manheim, Germany) using QuantiTect SYBR Green PCR Kit (Qiagen, Hilden, Germany) and gene-specific primers (QuantiTect Primer Assay from Qiagen) for Alkaline phosphatase (ALPL), Osteoclacin (BGLAP), Collagen I chain α1 (COL1A1), Caspase 3 (CASP-3), Interleukin-6 (IL-6) and Nitric oxide synthase 2, inducible (NOS2).

The protocol included a denaturation cycle at 95 °C for 15′, 25 to 40 cycles of amplification (95 °C for 15″, 55 °C annealing temperature for each target for 20″, and 72 °C for 20″). After melting curve analysis to check for amplicon specificity, the threshold cycle was determined for each sample, gene expression levels of the target genes were calculated by normalization to the reference gene GAPDH. The results were reported in terms of Relative value to the n100000 molecules of GAPDH.

2.8. *In vivo studies*

In vivo studies were performed in accordance with the Italian Law on animal experimentation, within the framework of projects approved by the Ethics Committee and the Animal Welfare Board of the Rizzoli Orthopaedic Institute and the Ministry of Health, as required by the current Legislative Decree (No. 26/2014), with authorizations **No. 44/2016-PR** for the local effect after implant in bone tissue (histocompatibility study) and authorizations **No. 106/2022-PR** for the antibacterial efficacy study.

The *in vivo* protocols were developed in accordance with the PREPARE guidelines (Planning Research and Experimental Procedures an Animals: Recommendations for Excellence) [58]. *In vivo* studies were performed onto customized materials appropriately miniaturized by ITC (5 mm height x 5 mm diameter) with the appropriate geometric and structural characteristics coated or uncoated to evaluate coating histocompatibility and osteointegrative properties and antibacterial efficacy. For both studies, rabbit animal model was chosen due to its bone architecture and immune characteristics, which provide a relevant approximation of human conditions in implant-related studies [59–60]. To further improve the quality of the studies, the *in vivo* research methodology was reported in the manuscript according to criteria set in

the Animal in Research: Reporting *in Vivo* Experiments (ARRIVE 2.0) guidelines [61].

For both studies, male New Zealand (NZ) white rabbits, sourced from an authorized supplier (Charles River, SAS France RMS) and weighing 2.81 ± 0.39 kg were used, housed in individual cages and fed with a standard pellet diet (Mucedola, Settimo Milanese, Milan, Italy) and water *ad libitum*.

After the quarantine period, the animals underwent a surgical procedure for implants placement. All surgical procedures were performed under general anaesthesia, induced by intramuscular injection of 44 mg/kg ketamine (Imalgene 1000, Merial Italy SpA, Assago-Milan, Italy) and 3 mg/kg xylazine (Rompun, Bayer SpA, Milan, Italy) and maintained with O2/air (60 %/40 %) mixture with 2–2.5 % sevorane (Sevorane, ABBOTT Srl, Latina, Italy) in spontaneous breathing by a facial mask.

During the post-operative period, the animals received analgesic therapy which comprised intramuscular injection of 1.5 mg ropivacaine hydrochloride (Ropivacaine Kabi 7.5 mg/mL—Fresenius Kabi Italia Srl, Isola della Scala VR) at the end of the surgical procedures; application of a 1/3 fentanyl-based transdermal patch (Matrifen50 μg/hour—-Grunenthal Italia Srl, Milan, Italy) and intramuscular injection of 50 mg/kg/day for 3 days of sodium metamizole (Farmolisina, Vetem SpA, Porto Empedocle—AG, Italy). For 5 days consecutively, only for the animal of the histocompatibility study, antibiotic therapy with 10 mg/kg of enrofloxacin (Baytril, Bayer S.p.A., Milano, Italy) was administered s.c.

The animals were housed in individual cages and underwent daily veterinary clinical examination in the first week and weekly thereafter throughout the study's duration. The animal welfare evaluation involved monitoring general and local conditions such as the mobility and functionality of the operated limbs, weight, major organ functions, food, and water consumption. If weight loss, infection, or surgical wound lesions were observed, the pharmacological and/or analgesic protocol was adjusted. Humane endpoints were established in advance: body weight loss greater than 20 %, severe limb injuries, fractures, or significant alterations in major organ functions. At the end of scheduled experimental times, pharmacological euthanasia was administered by intravenous injection of 2 mL of Tanax (Hoechst AG, Frankfurt-am-Main) after deep premedication with ketamine and xylaxine, as previously described

2.8.1. *In vivo assessment of histocompatibility and osteointegrative properties of nanostructured coatings (**No. 44/2016-PR**)*

Ten New Zealand rabbits were used for this assessment. No *a priori* statistical power analysis was performed, as the number of animals was determined in compliance with the recommendations provided by UNI EN ISO 10,993- Part 6. After the quarantine period, under general anaesthesia as previously described, after trichotomy and hind limb surface disinfection, a bilateral longitudinal cutaneous and subcutaneous incision was made until reaching the muscle layer, exposing the lateral distal femoral condyle surface. A low-speed perforation of the bone tissue was performed with tips of different diameters, accompanied by continuous irrigation with room temperature saline solution, resulting in a bone loss of 5 mm in diameter and 5 mm in depth. Implant randomization was not conducted as the right femoral condyle always received Ag/Bone coatings, while in the left condyle the uncoated substrate was implanted, according to the guidelines provided by the UNI EN ISO 10,993 –Biological evaluation of medical devices - Part 6 (2017): Tests for local effects after implantation. The materials were implanted by press fit. Then the surgical wounds were sutured layer by layer. Prior the end of the fixed experimental time (12 weeks), animals were submitted to intramuscular administration of 30 mg/kg oxytetracycline (Terramycin 100, Pfizer Italy, Italy) administered consecutively for two days, discontinued for ten days, and again administered for two more days, in order to mark the growing bone tissue at the level of the implants and to perform dynamic histomorphometric assessments.

Upon reaching the experimental time of 12 weeks, the animals were pharmacologically euthanized under general anaesthesia as previously described. Distal femoral epiphyses were explanted and a macroscopic evaluation of tissue reaction to the coating was performed focused onto the presence of hematomas, oedema, inflammatory or necrotic type reactions. The explanted bone segments were fixed, dehydrated, and finally embedded methacrylate-based solution. Once the resin polymerization process was completed, the specimens were cut transversely using the EXAKT Cutting and Grinding Systems (EXAKT Cutting and Grinding Systems, GmbH Apparatus GmbH & Co., Norderstedt, Germany). Histological sections from the central area of the implant were thinned and polished with abrasive papers using a polishing system (Saphir 550, ATM GmbH, Mammelzen, Germany) until a final thickness of 15 ± 5 μm. Unstained sections were observed under an optical microscope equipped with a fluorescence device (BX51, Olympus Optical Co. Europe GmbH, Germany) at 20x magnification for visualisation of the administered fluorochrome, and the corresponding images were acquired with the CellSense image analysis system (Olympus Optical Co. Europe GmbH, Germany) for dynamic histomorphometric analysis. Subsequently, these sections were stained with Toluidine Blue counterstained with Picrofucsin according to Van Gieson. Histological preparations were acquired by Aperio digital scanner as images in .svs format (AperioScanscope CS System, Aperio Technologies*, Vista, CA - USA),* later converted to .tif files at different magnifications. The semi-quantitative score provided by ISO 10,993–6:2017 (Annex E) for evaluation of inflammatory cell infiltrates, necrosis, neovascularization, fibrosis, and adipose tissue infiltration was applied on the histological preparations. On the stained and unstained histologic sections, the regenerative and osseointegrative process was also evaluated by measuring the following parameter as defined by the "American Society of Bone and Mineral Research (ASBMR)" [62] using ImageJ software (National Institutes of Health, Bethesda, MD, USA):

- Percentage of contact between the materials implanted in each defect and the bone tissue (Bone to Implant contact BIC, in %), expressed as the ratio between the perimeter of the material and the perimeter of bone-to-material contact.
- Mineral Apposition Rate (MAR μm/day): rate of mineralization of newly formed bone calculated as the ratio of the average distance between the two fluorescence bands of the same trabeculae (label #1 and #2 in the side image) and the number of days elapsed between the first and fourth marking. It represents the rate of deposition over time of bone matrix by osteoblasts which, by mineralizing, incorporates the fluorochrome used. Higher values of this parameter indicate a higher rate of deposition of new bone, which is indicative of greater osteoblastic activity conditioned by the topography of the implant and its chemical composition.
- Bone Formation Rate (BFR/BS μm3/μm2/day): expresses the measure of the amount of mineralized bone formed per unit area of trabecular bone per day. It is calculated by multiplying the value of MAR by the following formula:

$$MAR * (1 / 2\ sL.Pm / B.Pm\ +\ dL.Pm / B.Pm)$$

Where sL.Pm/B.Pm is the length of the single fluorescent band expressed relative to the length of the bone trabeculae on which it is present, and dL.Pm/B.Pm is the length of the double fluorescent band. Higher values of this parameter indicate the presence of more newly formed bone that is mineralized and therefore mature

2.9. *Microbiological set-up for in vivo antibacterial assessment*

2.9.1. *Bacterial culture preparation*

For the *in vivo* assessment of the antibacterial properties of the

coating, we developed an experimental procedure aimed at implanting the substrates in animals after immersion in a bacterial suspension that was optimized and prepared as follows. *S. aureus* USA 300 was streaked onto Tryptic Soy Agar (TSA) plates and grown at 37 °C overnight. One single colony was cultured in Tryptic Soy Broth (TSB) and grown overnight at 37 °C in a shaking incubator. To obtain mid-logarithmic phase bacteria, a 1/50 dilution of the overnight culture was incubated for 2 h at 37 °C. Bacterial cells were pelleted and washed three times with Phosphate Buffered Saline (PBS) and then resuspended in NaCl 0.85 %. Bacterial concentration was adjusted in NaCl 0.85 % to obtain a final concentration of 5×10^5 Colony Forming Unit (CFU) mL^{-1}. 0.1 mL aliquots were finally prepared for the immersion (and bacterial adhesion) of the substrates used for the *in vivo* experiments.

2.9.2. *In vivo antibacterial efficacy of the nanostructured silver and silver/bone apatite coatings (**N° 106/2022-PR**)*

To investigate the antibacterial activity of the developed nanostructured coatings, another specific research project was approved by the Animal Welfare Board of the Rizzoli Orthopaedic Institute and authorized by the Ministry of Health, (Authorization code N° 106/2022-PR). *A priori* power analysis was performed using G*Power software (v.3.1.9.2, Germany). Assuming a power of 1-β = 0.80, a type I error probability α= 0.05, and an effect size $f > 0.55$, it was estimated that an = 5 animals per experimental group were required for the evaluation of the nanostructured coatings. In this experimental set-up, the effectiveness of the silver and silver/bone apatite coatings was evaluated in a setting that tried to mimic the device contamination occurrence. Indeed, to understand and assess the influence exerted by the bone apatite component in the nanostructured coating, full silver nanostructured coatings were also investigated.

The porous coated and uncoated material with the same dimensions previously reported (5 mm x 5 mm), were soaked in 0.1 mL suspension of USA 300 bacterial cells (prepared as described above) for 20 min before bone implantation. Three experimental groups ($n = 5$ rabbits for each group) were set-up: **Ag-Bone Group, Ag-Group,** and **Control Group** (uncoated porous material). Fifteen New Zealand rabbits were used. Animals were allocated to treatment groups according to the order of surgical sessions. While no individual randomization was performed, this approach minimized potential temporal and procedural bias. Under general anesthesia, as previously described, a defect of 5 mm in diameter and 5 mm in depth was created in the intercondylar region of the right femur, and the soaked substrates were implanted in the created defect by press-fit. During the postoperative period, the animals were housed in individual cages and underwent daily veterinary clinical examination and by recording body weight and any symptoms using the appropriate evaluation form.

After 1 week from surgery, while keeping animals in deep sedation, two blood samples (about 5 mL each) were harvested from the medial auricular artery of each animal, for aerobic and anaerobic blood cultures to detect the presence of bacteria systemically. After euthanasia, macroscopic control of bone and soft tissues adjacent to the surgical site of implant was performed and then the right femurs were explanted under sterile conditions. Through a middle epiphyseal section of the femur, the porous materials were removed in sterility, and i) a microbiological swab of the bone tissue in contact with materials was performed; ii) one half of the femoral condyle was devoted to the evaluation of the MRSA load at bone level and iii) on the remaining hemi-condyle of the femur, qualitative histological evaluations and semiquantitative score as described by Smeltzer et al. [63] was executed to assess the presence of the inflammatory response induced by the bacteria contamination (acute and chronic intraosseous inflammation, periosteal inflammation and bone necrosis). Therefore, these latter specimens were fixed in formalin, decalcified, dehydrated and embedded in paraffin. Samples were cut with microtome to realize cross sections of 5 ± 1 μm in thickness (Microtome Micron HM 340E), which were stained with Hematoxylin/Eosin. The histological sections were digitalized with scanner (Aperio Scanscope CS System, Aperio Technologies, Vista, *CA* - USA) at maximum resolution (1781 × 1467 pixels) to evaluate the bone tissue response to coatings.

2.9.3. *Quantification of S. aureus USA 300 cells after in vivo infection*

The blood cultures were diluted 1/5 in TSB and incubated under aerobic and anaerobic conditions for 7 days. Swabs of the intramedullary bone, the hemicondyle, and the cage were removed, placed in sterile tubes with NaCl 0.85 %, and sonicated for 3 min at 30 kHz (Branson 2510 sonicator). Previous studies have suggested the use of sonication as an effective method for recovering viable bacterial cells from metal surfaces [64,65]. Serial 10-fold dilutions of each suspension were performed to evaluate the bacterial loads by counting the number of CFU on TSA plates after 24 h at 37 °C. The complete *in vivo* experimental procedure is displayed in **Supplementary File, Figure A**.

2.10. *Statistical analysis*

Statistical analyses were performed using GraphPad Prism software (version 9). Data are presented as mean ± standard deviation (SD). For *in vitro* experiments with MG63 cell line (cytotoxicity tests) and microbiological assays, three biological replicates were used. For *in vitro* bioactivity tests with primary human osteoblasts, two biological replicates were used, each with multiple technical replicates.

In vitro data from cytotoxicity and microbiological assay were analyzed using one-way ANOVA followed by Sidak's post-hoc test, while data from bioactivity study were analyzed with two-way ANOVA, with material type and incubation time as factors, followed by Sidak's post-hoc test for multiple comparisons. Normality of data distribution was assessed using Shapiro-Wilk test, and residuals were examined to confirm the assumption of homogeneity of variance.

For *in vivo* histomorphometric analysis (static and dynamic results), a paired *t*-test was used to compare the two materials, as both were implanted in contralateral sites within the same animal. For the analysis of the Smeltzer score results, a one-sample *t*-test was performed after confirming normality of the data distribution. A significance level of $p <$ 0.05 was considered statistically significant in all tests.

3. Results and discussion

3.1. *Design and additive manufacturing of samples for in vitro and in vivo test*

Two distinct kinds of samples were manufactured starting from the same porous gyroid deformed structure with nominal CAD dimensions as follow (**Supplementary File Figure B**):

- Round cross section of gyroid bars with thickness of 0.5 mm
- Vertical Pore size 2.6 mm
- Horizontal pore size 1.3 mm
- Shell thickness around the samples 0.6 mm
- Porosity of *in vivo* samples: 76.75 %
- Porosity of *in vitro* samples: 78.34 %

3.2. *Preliminary assessment of the properties of ag-bone films in comparison with ag-films*

After the pre-screening that allowed us to select the optimal composite target and deposition conditions, we proceeded to the characterization of the morphological and compositional characteristics of the Ag Bone coatings. All data are reported in the supplementary materials.

When deposited onto flat substrates, bone-silver apatite coatings showed a morphology intermediate between silver and bone apatite films, where some larger grains (1–2 μm diameter) grow sparsely over a finer layer of round aggregates having nanosized diameters (Supplementary File, **Figure C**). Coatings showed high surface uniformity, and

no defects (cracking, fissuring detachments) were noticed in any part of the coated substrates. The same morphology is maintained when the coating is deposited on the 3D printed prostheses.

XRD (**Supplementary File, Figure D**) spectra show that both coatings are mainly characterized by the presence of metallic silver. Due to the low thickness of the films, and the low crystallinity of the apatitic phase, its presence is not evidenced by XRD spectra.

However, EDS analyses, performed on silver (**Supplementary File, Figure E**) and silver-bone apatite films (Fig. 2), showed that, while the first were only constituted by silver, Ag-Bone coatings are characterized by the larger aggregates constituted by bone apatite, immersed in an underlying finer layer mainly made of silver. Indeed, although signals of *Ca* and P are detected in all areas of the sample, they are significantly stronger in the larger grains, where Mg and Sr can also be detected. This indicates that not only the main apatitic phase, but also trace ions present in bone are transferred to the coating, as previously found for coatings of bone apatite alone [28,54].

3.3. Coatings compositional and morphological characterization

FEG-SEM (**Supplementary File Figures F** and **G, and** Fig. 2) show that the deposition is conformal and the coatings are submicrometric, no alterations were caused in the morphology of the scaffold, neither on their surface, nor in the inner areas of the scaffold.

When analyzed at larger magnification (**Supplementary Figure G**), film showed a nanosized surface morphology, with larger apatite aggregates emerging from the top of a finer silver layer, as in the case of deposition onto flat substrates. Our previous results show that coatings having high surface roughness and nanosized morphology can promote MSCs adhesion to substrate, early proliferation and differentiation [28, 66]. At the same time, nanostructured surface morphology permits a more finely tuned control over silver release [34]. EDS maps demonstrate that the coatings do homogeneously cover all the substrate, confirming the absence of defects (Fig. 2c). No differences in ions type and/or distribution was observed with respect to deposition onto flat samples (Supplementary material). EDS quantification (Table 1) shows that silver content is higher in Ag films, consistently with the fact that Ag-Bone is a two phase coating. The presence of bone-mimetic ions in the coatings is confirmed by ICP-OES that shows that the coating is constituted by silver (2,74 ± 0,12 mg/L), and bone-mimetic ions (Ca: 14,43 ± 2,94 mg/L; P 3,83 ± 0,59 mg/L; Mg 0015 ± 0,01 mg/L; Sr 0,02 ± 0,01 mg/L). Interestingly, data show the presence of Mg and Sr in Ag-Bone films, in concentrations about 0.15 and 0.02 mg/l, indicating that trace ions in bone apatite are preserved by the deposition and transferred to the coating.

Table 1
Initial and residual silver content following 7 days incubation in PBS, as assessed by EDS.

Residual Silver (wt %)		
	t0	7d
Ag	84.56±3.33	54.45±14.00
Ag-Bone	55.51±0.25	25.85±13.78

FIB-SEM analysis shows that thickness of the silver coating in the Ag sample is *ca.* 100 nm in thickness (Fig. 2c-e). This coating covers homogeneously the surface of the substrate, without defects or scaling. For the Ag-Bone films, two layers can be distinguished: one bright layer *ca.* 50 nm-thick that corresponds to silver (Fig. 3b-c and e), and a darker layer between the silver and the substrate that is only approx. 10 nm thick. This interlayer was too thin for the detection of *Ca* and P using EDS, however, their low contrast compared to the silver coating on top

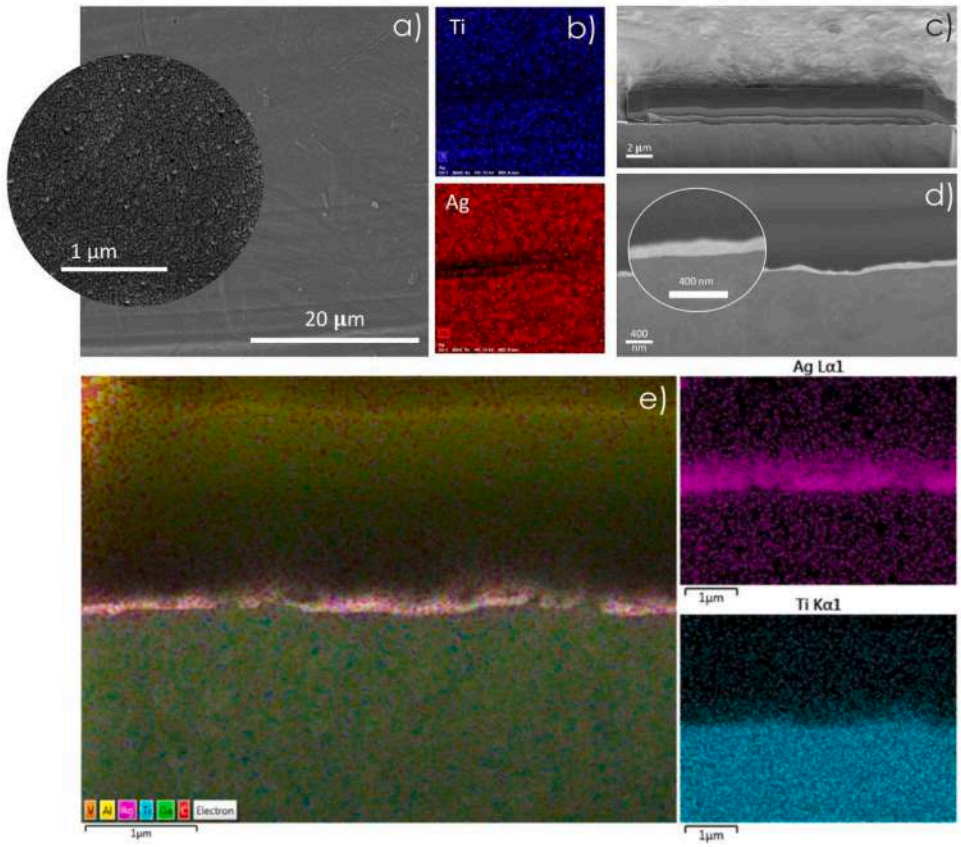

Fig. 2. Silver coatings. a) morphology at FEG-SEM and b) EDS maps on the surface show high homogeneity and absence of defects. (c, d) FIB cross section of the coatings show a nanoscale thickness of about 60 nm. e) EDS maps on the cross-section confirm that coatings are constituted by silver.

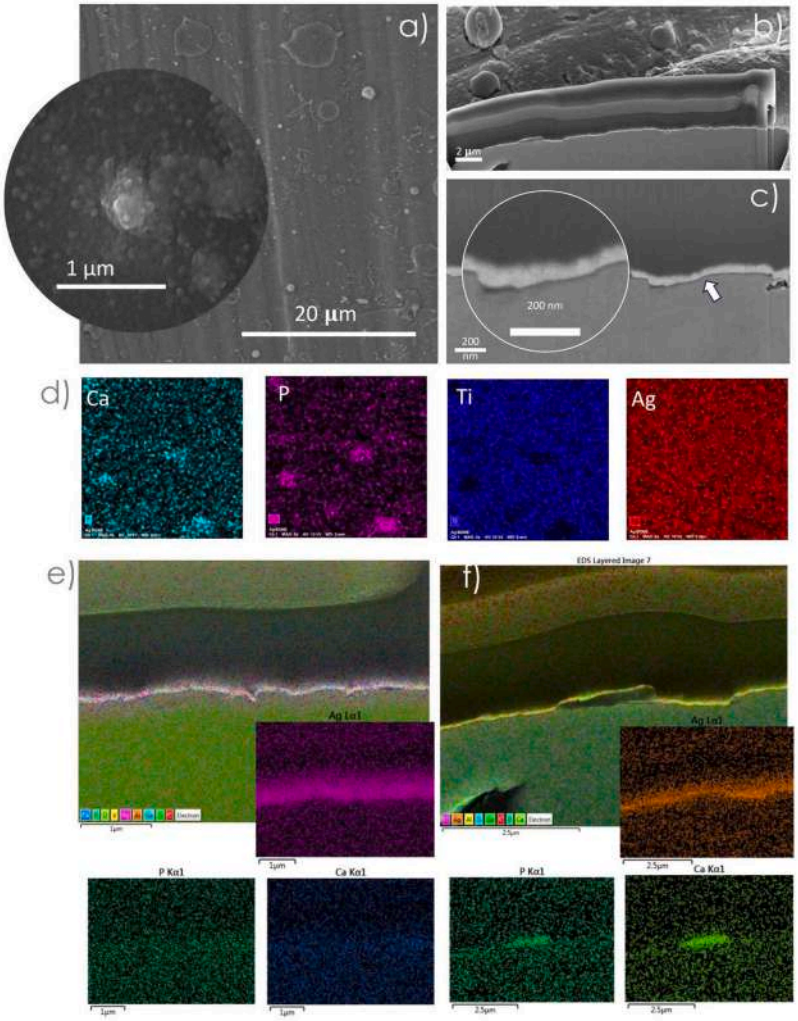

Fig. 3. Silver bone apatite coatings. a) morphology at FEG-SEM and b,c) FIB cross section of the coatings showing a nanoscale thickness of about 100 nm. Different from Ag films, Ag-Bone coating is constituted by two layers, comprising one darker (arrow) in contact with the substrate, that is compatible with a CaP layer. d) EDS maps on the surface, showing high homogeneity and absence of defects. (e) EDS maps on the cross-section confirm that coatings are constituted by silver. Here, *Ca* and P are hardly distinguishable, due to the very low thickness on the film. However, their presence is clearly seen in the presence of larger aggregates (f).

and the metal substrate at the bottom is consistent with a composition of apatite. Furthermore, in certain regions this layer was significantly thicker, reaching up to ~250 nm thick where both *Ca* and P were detected by EDS (Fig. 3f). This suggests that while apatite is mostly present as a 10 nm interlayer between the silver and the substrate, it also forms larger and thicker aggregates.

EDS coupled with FIB shows that both coatings are mainly composed by silver. Due to the low thickness of the coatings, the presence of interlayers cannot be clearly demonstrated, although overlapping between silver and Ti signal suggests their presence, as already found for IJD coatings on Titanium alloy [36].

Combining data on the surface and the cross-section, we can observe that silver is present in all areas of Ag-Bone samples, and a Ag thin layer covers even the larger CaP aggregates. This is a result of the deposition process, where the thin CaP layer deposited on the silver target is exposed to ablation first (see Fig. 1), so it is consumed in the first phases of deposition. Because of the low thickness of the CaP layer in the composite target, even in the first stages some silver is ablated also in the first stages, ensuring antimicrobial action and avoiding mismatch due to the presence of separate overlapping layers.. Then, only silver remains, hence the outer nanometric layers of the coatings are constituted by silver only. Hence, although the total content of silver is higher in the Ag samples, Ag signal is clearly detected by EDS in all areas of the sample.

When immersed in PBS, coatings progressively dissolve, releasing silver and, in the case of Ag-Bone, also bioactive ions (Table 2). ICP-OES data show that the release of silver starts upon immersion and remains essentially constant in the first 24 h. A sustained silver release is measured also at 7 days, for both coatings. As expected, silver release is essentially identical in the first 24 h between Ag and Ag-bone films, while differences are observed at 7 days, when release in Ag-Bone is lower, consistently with the gradient nature of the film, that has a higher concentration of silver in the surface. Consistently, release of calcium is constant for the first 24 h, then sharply increases at 7 days. Indeed, as shown in EDS (Fig. 2 and Fig. 3), the outer parts of the films are constituted by silver only, the inner by both silver and bone apatite ions.

After immersion in PBS, residual presence of the coatings is observed

Table 2
Ion release from the coatings incubated in PBS at different timepoints.

	Silver release (mg/l)			Calcium release (mg/l)		
	3h	**24h**	**7d**	**3h**	**24h**	**7d**
Ag	0.51 ±0.014	0.53 ±0.05	2.97 ±1.29	/	/	/
Ag-Bone	0.52±0.01	0.52 ±0.05	1.75 ±0.05	43.2 ± 2	43 ±2.12	92.2 ± 5

by FEG-SEM and EDS. SEM observation show that the coating is still present in both Ag and Ag-Bone films, although dissolution is heterogeneous and higher in some areas (Fig. 4).

In spite of this difference, residual presence of Ag in observed in all areas of the coatings, indicating that the coatings dissolve and do not delaminate. EDS quantification, in particular, show that over 50 % of the initial content of the coating is retained, and that the amount of silver, in the areas subjected to highest dissolution is of about 50 % of the initial content for Ag and about 20 % of the initial content for Ag-Bone, suggesting a higher durability of Ag films (Table 1). Notably, since salts deriving from crystallized PBS are present over some areas of the samples, although their presence does not hamper detection of silver, it could reduce the signal, so residual silver content might be underestimated.

3.3. Application to a real scale prosthesis

When coatings were deposited onto real-scale prosthesis (Fig. 5–8), good results were found in terms of surface coverage, since the coatings reached deep areas of the prostheses, negligent of the deposition direction. In both cases on the deposition surface, the coatings showed high homogeneity and the presence of apatite and silver clusters, as observed before. Instead, differences were observed in the efficiency of deposition in the center of the prosthesis, depending on the plume angle (EDS data are in Table 3 **and Supplementary File, Figure I)**.

For deposition at 0–180°, the coating was uniform and showed no defect, both on the surface and in the inner areas. Progressing toward inner rings, the coatings morphology became finer, the aggregates smaller a progressive reduction was registered in the coating thickness, as indicated by the substrate becoming progressively more visible. In the center of the prosthesis, the coating could not be detected.

Observing the prosthesis surface deposited at 90–270° angle, a high uniformity was noticed, and no defects were observed. No alterations were observed in the substrate morphology, obtained through 3D printing and optimized for the prosthesis's integration.

Although aggregates were smaller and less easily detectable than in the 0–180° setup, the coating was visible in all areas of the prosthesis, including the center, as shown by EDS. The coating was highly uniform, and no differences were assessed when areas at the same distance from the plasma plume were observed (Fig. 6**a**). EDS showed that the amount of silver was maximum on the deposition surface, as expected, and progressively decreases while moving towards the center, *i.e.* farther from the plasma plume. The amount of silver correlates with the thickness of the coating; hence, we inferred that the coating thickness progressively decreases, which correlates with the characteristic behavior of plasma-assisted deposition techniques. However, different from traditional plasma-assisted thin films on complex substrates, where shadowing is relevant, here we did not observe any uncoated areas, and the coating reached all spots in the prostheses, indicating successful deposition.

Since the 90–270° inclination has higher easiness of deposition and optimal substrate coverage, it was chosen as the best deposition procedure, (Fig. 7**)**.

Overall, like all plasma-assisted techniques, IJD deposition results in a different morphology of the coating in the different areas, depending on the distance and the angle formed with the plasma plume. Many techniques, such as plasma-spray and magnetron sputtering cause significant shadowing, so many areas remain uncoated. In our case, we demonstrated that we can completely avoid shadowing. In addition, as far as all areas of the prostheses are coated and exert antibacterial action, the different characteristics between the surface and the inner core are not detrimental, as silver coating is thicker in the outside areas of the prostheses, which are in first contact with bacteria and more exposed to interaction with body fluids. This means that the coating is thicker where there is more need for antibacterial action and where more dissolution is to be expected.

3.4. Biological investigations

3.4.1. Antibacterial efficacy in vitro

Results of the impact of Ag and Ag-Bone coatings on the planktonic growth of bacteria are shown in Fig. 9 and in **Supplementary Table 2**.

Silver and silver-bone apatite films showed >4 log and >6 log reduction (equal to >99.99 % CFU reduction), respectively, for all the three tested strains, indicating that both coatings provided excellent antibacterial activity *in vitro*. Nanostructured silver coatings were shown to have higher efficacy against gram-negative strains compared to gram-positive strains, both in terms of planktonic growth and biofilm

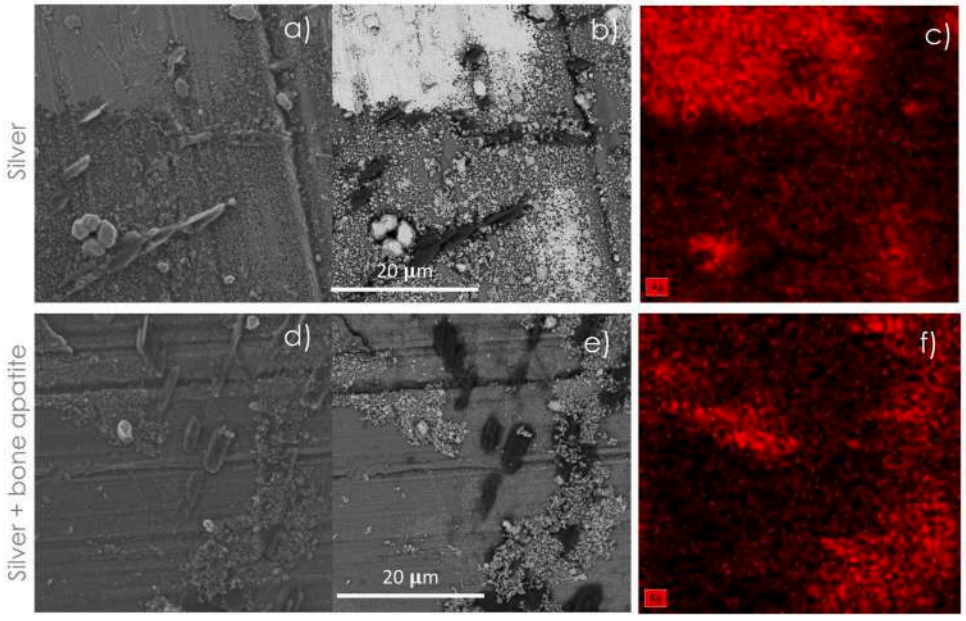

Fig. 4. Ag and Ag-bone coatings following 7 days immersion in PBS, as observed by FEG-SEM: secondary electrons on a) silver and d) silver-bone apatite; backscattered electrons on b) silver, e) silver-bone apatite and EDS maps on c) silver, f) silver-bone apatite.

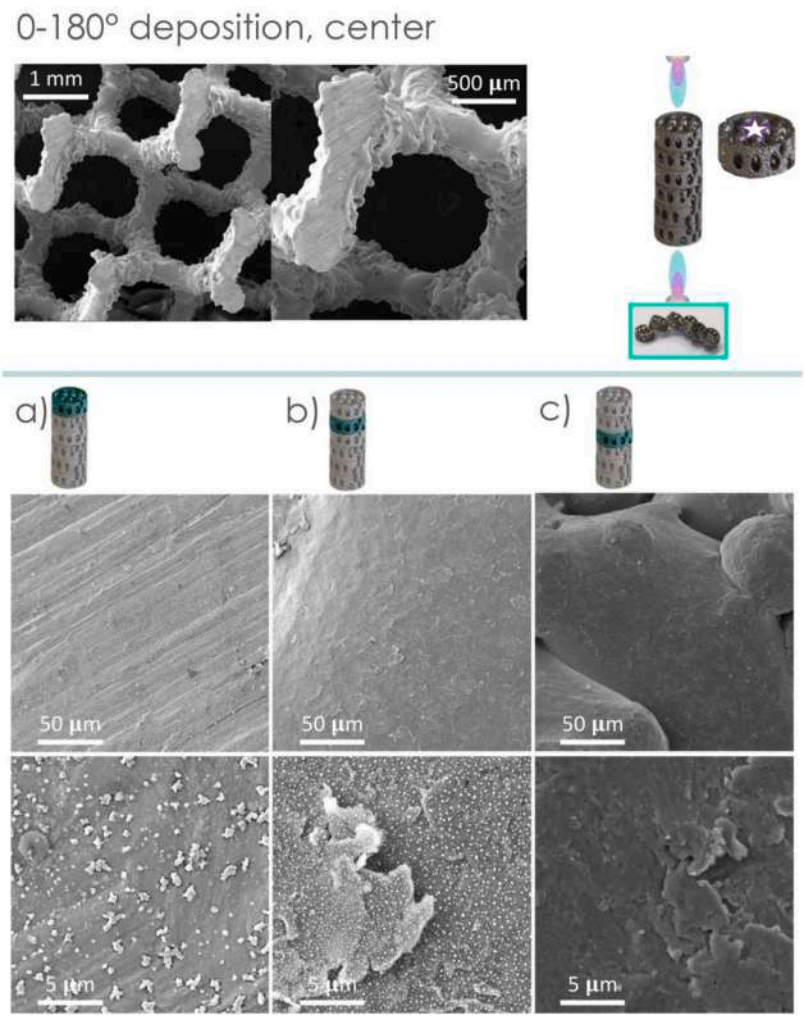

Fig. 5. Deposition along the 0–180° direction. Coating morphology is observed at different magnification and depth with respect to the prosthesis surface.

Table 3
Silver amount in different areas of the prosthesis, depending on deposition orientation. Silver content is taken as representative of the presence/absence of the coating, being the most abundant element in the coating, and correlates with its thickness. For the exact sampling position, see schemes in Figs. 6,7,8.

0–90°		
Surface (deposition surface)	1.5 depth	3 cm depth
52.91 ± 2.51	6.34 ± 0.92	/
90–180°		
External surface (deposition surface)	Inner porous area close to surface	Inner porous area Center
60.42 ± 2.43	16.78 ± 0.72	2.18 ± 0.30

formation as demonstrated by SEM analysis in a previous study [34], indicating that antibacterial activity is associated to both direct contact with the coating and the metal ion release. Indeed, gram-negative bacteria are often more susceptible to silver due to their thinner peptidoglycan layer and the presence of an outer membrane rich in negatively charged lipopolysaccharides (LPS), which can attract and bind positively charged silver ions. In contrast, gram-positive bacteria have a much thicker peptidoglycan layer, which may act as a partial barrier, slowing the diffusion of silver ions and nanoparticles [67]. However, silver activity is also strain-specific and influenced by the genetic composition of each bacterial isolate, as reflected in our results, which demonstrate reduced sensitivity to silver in the MRSA strain compared to the *S. aureus* ATCC reference strain [68] In the case of *E. coli* ATCC 8739 and MRSA USA 300, Ag exerted a higher antibacterial activity compared to Ag-Bone, probably because the bone apatite slightly interferes with the activity of the silver coating.

3.4.2. In vitro cytotoxicity evaluation of silver and bone apatite/silver nanostructured coatings

The effect of nanocoatings on the proliferation of osteoblast-like cells (MG63) is reported in Supplementary File **Figure JA**. Statistical analysis highlighted significant differences among Ag and Ag-Bone compared to the Ti substrate and CTR-, with lower proliferation values ($p < 0.001$) for nanocoatings, and between Ti and CTR- ($p < 0.001$). At 72 h, a significant difference was also observed between CTR+ and all conditions ($p < 0.001$). Nevertheless, the proliferation values for the investigated nanocoatings were higher than 70 % compared to CTR-, suggesting the absence of cytotoxicity according to UNI EN ISO 10,993. This result was further confirmed by quantifying the neutral red vital dye (Supplementary File, **Figures JB**) and by the quantification of the LDH enzyme released in the culture supernatant. The values of LDH were close to zero for both nanostructured coatings, indicating an absence of LDH release, and might be inferred that the silver nanoparticles did not induce damage to the cell surface membrane. The results confirm our previous findings regarding nanostructured silver coating and suggested that the choice of deposition technique and related parameters produce a uniform and balanced coating, where the silver component exert its

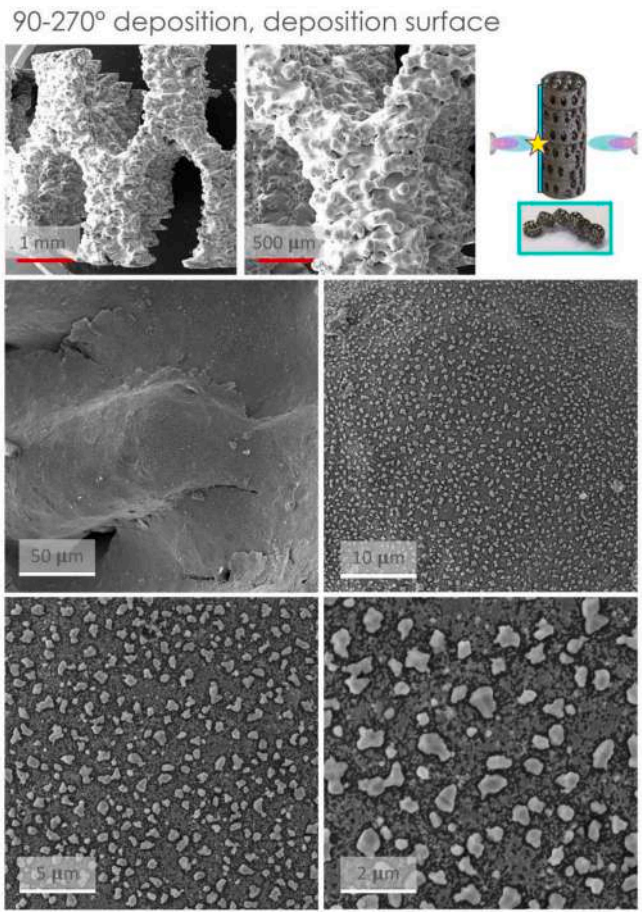

Fig. 6. Deposition surface of the 90–270° angle.

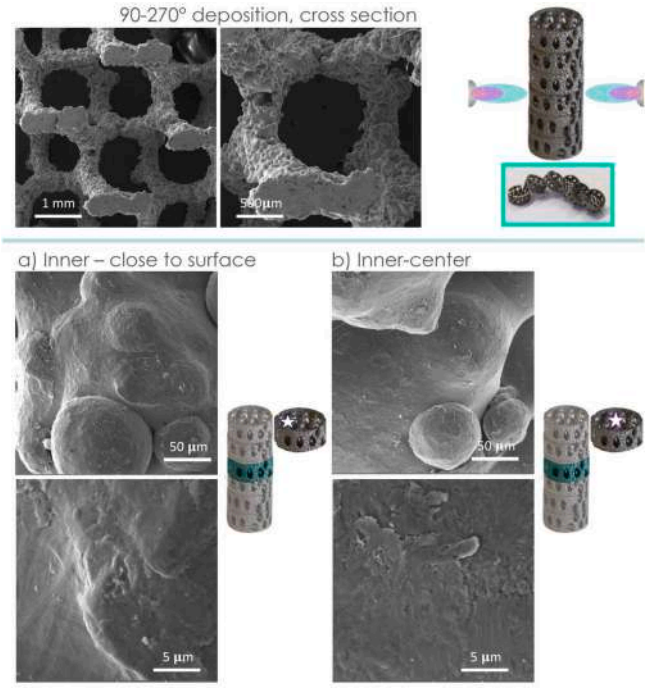

Fig. 7. Deposition at different depth for the 90–270° angle.

antibacterial activity (results obtained from *in vitro* antibacterial investigations), without significantly altering some of the key cellular functions [44]. Finally, current results suggested a similar trend also for combined Ag-Bone coatings. The numerical data obtained from each test - WST-1, LDH and Neutral Red - are reported in Supplementary File Table 3

3.4.3. In vitro bioactivity study on the combined bone apatite/silver nanostructured coating

In the complex management of vertebral reconstruction, phenomena such as subsidence, implant loosening, and the onset of infection unfortunately represent real and well-described complications [69,70]. An approach that addresses these three key points would provide an effective tool to increase the long-term reliability of reconstructive surgery in spinal applications as well as in numerous other orthopedic applications that share the same needs. However, the integration of these elements requires further investigation and analysis to understand how effectively they perform together. To address this, enhanced experimental setups were made, starting with the culturing of primary human osteoblasts on 3D printed custom nanocoated porous substrates, as shown in Fig. 10**A**. The results regarding metabolic activity, investigated using Alamar Blue assay, are reported in Fig. 10**B** These results showed an increase in metabolic activity from 3 to 7 days for nHOb grown in direct contact with Ag-Bone, although this increase was not statistically significant. Significant differences were observed for the Ti substrate between 7 days ($p < 0.005$) and 14 days ($p < 0.05$) compared to 3, likely benefiting from the porous structure of the additive-manufactured substrate. At 3 and 7 days, no significant differences were detected between coated and uncoated substrates, while at day 14, a higher metabolic activity was measured for the uncoated substrate compared to Ag-Bone ($p < 0.05$). Considering the presence of silver and the susceptibility of primary hObs to silver particle-mediated inhibition, the metabolic results showed a positive trend. ELISA tests were additionally performed to evaluate the production of some of the main markers of osteoblasts differentiation to understand how silver impacts on these cellular activities. Osteocalcin and alkaline phosphatase (ALP), which are key proteins in the bone formation and mineralization process, where investigated as early marker of differentiation, while Type I collagen, the major components of bone matrix, was used as a late indicator of differentiation. For osteocalcin, an increase in protein production was detected from 3 to 7 days for Ag-Bone ($p < 0.0005$). No differences were detected between coated and coated substrate, with comparable values between materials (Fig. 10**C**). The production of ALP was higher for the coated substrate as showed by Fig. 10**D** although the statistical analysis did not highlight significance in comparison to the uncoated substrate except at day 14 (Ag-Bone *vs* Ti-substrate: $p < 0.05$). Similarly, for Type I collagen, no significant differences were detected at any time point or between the coated and the uncoated substrate (Fig. 10**E**).

The obtained results are encouraging as they confirm that the IJD deposition technique produce a uniform nanocoating with controlled silver release, balanced by the apatite component, thus avoiding the toxicity effects on cells frequently reported with other types of nanosilver coatings [71]. These findings can be explained by the nanoscale surface morphology of the coatings, where the increased surface area combined with the apatite components improves surface properties, i.e. wettability, adsorption of hydrophilic proteins, thereby promoting osteoblast activity while balancing the presence of silver. A similar trend was observed by Wu *et al.*, who studied 3D-printed Ti-6Al-4 V implants coated with copper and strontium combined with natural polymers (alginate and dopamine). Consistent with our findings, the osteogenic activity of MC3T3-E1 cells was not inhibited but enhanced on the coated materials, as shown by the expression of specific genes related to bone formation (RUNX2, COL-1, OPN), without a significant impact on pro-inflammatory pathway (MIF, NF-kB, and IKK) [72].

Indeed, from a catabolic perspective, the production and release of

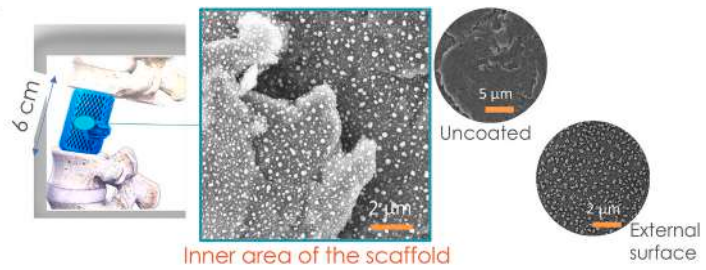

Fig. 8. Scheme of optimized deposition.

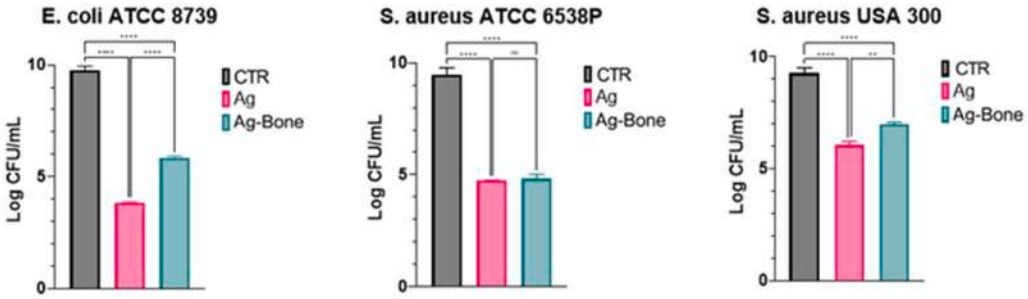

Fig. 9. Antibacterial activity of porous cylinders with (Ag and Ag-Bone) and without (CTR) coating against *E. coli* ATCC 8739, *S. aureus* ATCC 6538P, and Methicillin-Resistant *S. aureus* USA 300 after 8 h of incubation. ns: *: $p > 0.05$; **: $p < 0.01$; ****: $p < 0.0001$.

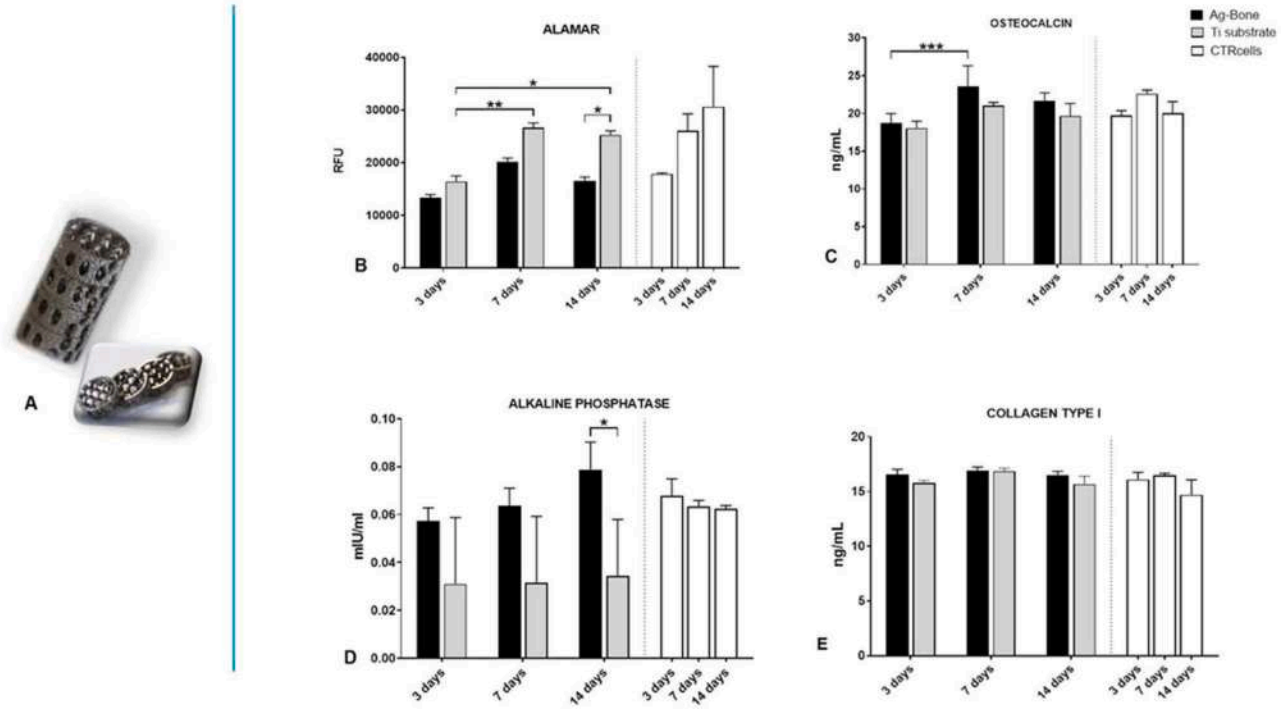

Fig. 10. In figure A visual macroscopic image of 3D printed titanium substrate is shown both as a singular element and as an assembled stackable element to reproduce the full-scale prosthesis. The highly porous structure with burr-like appearance is clearly recognizable. The histograms reported in Figure B-E refers to the Alamar Blue assay (Figure B) and ELISA assay for osteocalcin (Figure C), alkaline phosphatase (Figure D) and Type I collagen (Figure E). The measurements were performed by two biological replicates and data are reported as Mean ± SD (* $p < 0.05$; **, $p < 0.005$; ***, $p < 0.001$).

Caspase 3 and Interleukin 6 were consistently and significantly lower on coated substrates compared to uncoated material. This further confirms the hypothesis that the proper combination of rough surface morphology and nanocoating elements deposited with IJD can balance the potential toxic effect of silver.

Caspase enzymes are responsible for phenomena such as DNA fragmentation, chromatin compaction and cell fragmentation, thus playing a crucial role in apoptosis events. Caspase 3 is often referred to as the "cell death executioner" due to its pivotal involvement in the process. Indeed, once activated, Caspase-3 cleaves structural and regulatory proteins, leading to programmed cell death [73]. Otherwise, Interleukin-6 represents one of the most important mediators of

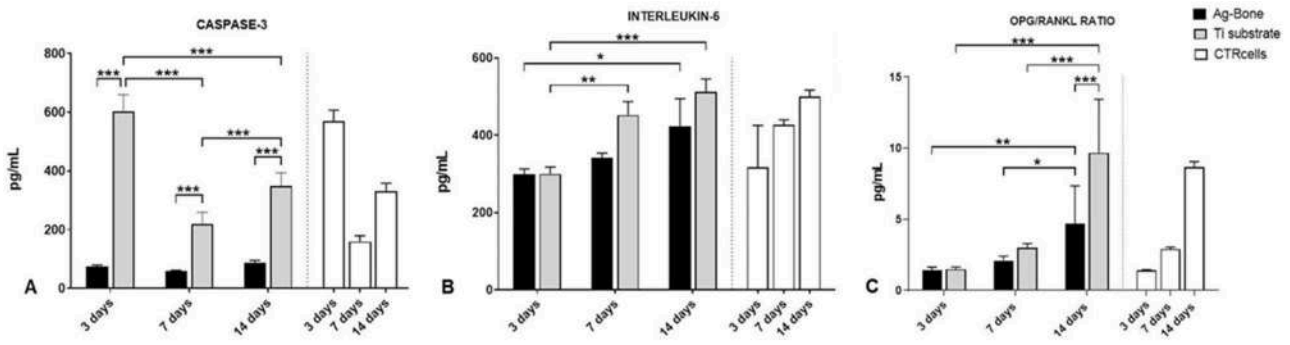

Fig. 11. Histograms related to ELISA results for Caspase 3 (Figure A), Interleukin −6 (Figure B) and for OPG/RANKL (Figure C). The measures were performed onto two biological replicates and data are reported as Mean ± SD (* $p < 0.05$; **, $p < 0.005$; ***, $p < 0.001$).

inflammation. The histogram shown in Fig. 11**A** reported a significantly higher content of Caspase 3 at each experimental time point for the uncoated Ti substrate compared to Ag-Bone ($p < 0.0001$) thus suggesting that the silver in the coatings did not increase the apoptotic events. Regarding IL-6, no significant differences were detected at any time points between coated and uncoated substrate (Fig. 11**B**). A final and crucial confirmation, came from the OPG/RANKL ratio, which reported positive results, consistently above one, also for the coated substrate indicating a tendency towards the reparative/regenerative process rather than towards bone resorption activity. Moreover, the values showed a progressive increase over time, suggesting that the osteoblasts maintained a homeostatic and regulatory role in modulating bone turnover (Fig. 11**C**) [74].

Our results are consistent with those reported by Castiglioni S. et al., who found that osteoblast-like cells (Saos-2) and primary human bone marrow mesenchymal stromal cells (hMSCs) are relatively resistant to the cytotoxic effects of silver nanoparticles, with average size comparable to those in our coatings (35 nm). According to Castiglioni, the toxic effect of silver is dose-dependent, and when silver is below this toxic levels it does not interfere with the cellular response to osteogenic stimuli [75]. Furthermore, the authors propose a cellular adaptive mechanism to silver nanoparticles through the activation of a stress response, hypothesizing the up-regulation of heat shock protein 70 (hsp70). This protein interacts with key regulators of various signal transduction pathways that govern cell proliferation, differentiation, and death. Additionally, Castiglioni et al. has reported that elevated levels of hsp70 protect against apoptosis by inhibiting both caspase-dependent and caspase-independent pathways, which may also explain the results obtained for Caspase-3 and IL-6.

To complement the protein-level analysis, we further investigated the expression of the same markers at the molecular level. While protein synthesis showed only minor variations between the Ti substrate and Ag-bone, gene expression analysis identified significant differences across all three anabolic markers. Specifically, a notable up-regulation was observed in the Ti group compared to Ag-bone. Nevertheless, gene expression remained consistently detectable in the Ag-bone group, showing a progressive increase from day 7 to day 14 for both ALPL and BGLAP, whereas COL1A1 did not exhibit a statistically significant change over time (Fig. 12**A, B and C**).

To assess potential cytotoxic and pro-apoptotic effects of the silver-based coating, Caspase-3 expression was also evaluated (Fig. 12**D**). The results indicated that silver ion release from the Ag-bone coating was effectively controlled, with gene expression levels lower than those observed for Ti at both time points. Similarly, IL-6 gene expression was comparable - or even lower at 14 days - in the Ag-bone group compared to Ti, indicating a normal cellular behavior and an absence of pro-

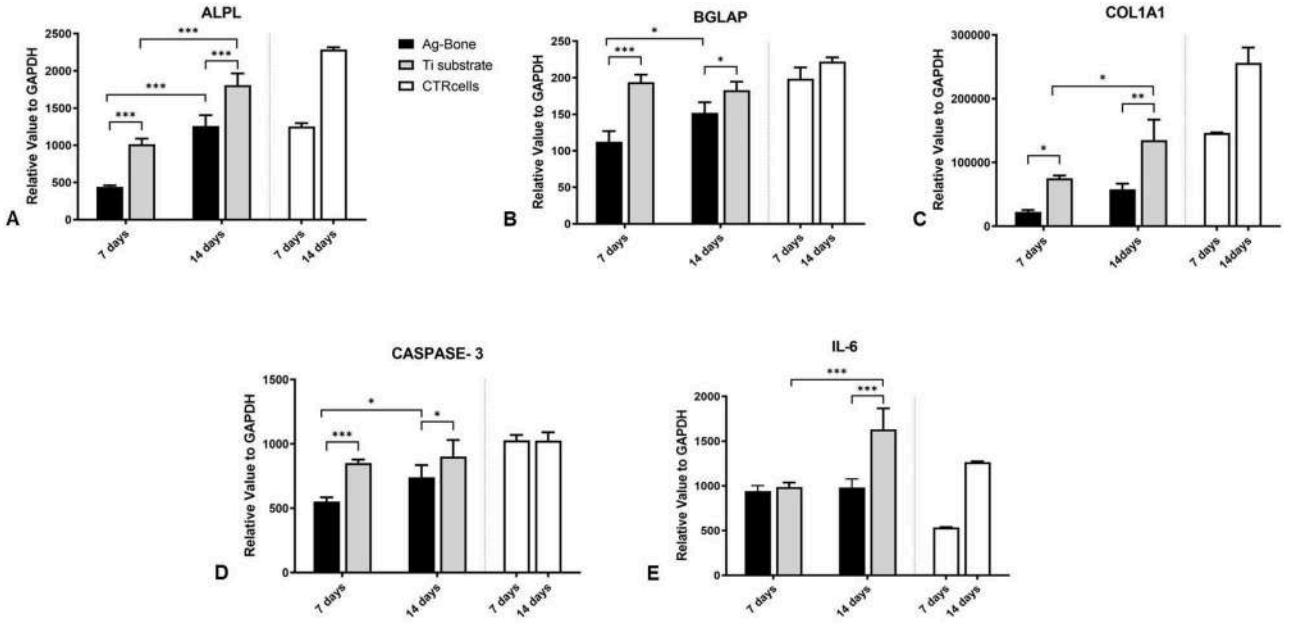

Fig. 12. Histograms of ALPL (**A**), BGLAP (**B**), COL1A1 (**C**), CASPASE-3 (**D**) and IL-6 (**E**) genes expression after 7 and 14 days of culture of nHOB onto Ag-Bone and Ti-substrate. Data are reported as mean ± standard deviations (SD) at a significance level of $p < 0.05$ (*$p < 0.05$, ** $p < 0.005$, *** $p < 0.001$).

inflammatory response (Fig. 12**E**). We also investigated the gene expression of NOS2, (also known as iNOS), an enzyme responsible for producing nitric oxide (NO), a key signaling molecule involved in immune response, inflammation, and oxidative stress. High silver ion release can induce oxidative stress, potentially leading to NOS2 overexpression, which contributes to the creation of an inflammatory microenvironment. However, in our cells culture with both Ag-bone and Ti, no NOS2 expression was detected as indicated by very high cycle threshold (Ct) values (above 35) (data not shown). This further confirms that the silver content in the Ag-bone does not induce a cytotoxic response. Altogether, these findings suggest that the antibacterial and osteoinductive coating not only preserves osteoblast viability, but may also contribute to a balanced osteogenic and immunomodulatory environment, promoting favorable integration at the tissue-implant interface. Perhaps Ag-Bone does not disrupt the osteoblasts' physiological signaling balance; rather it may promote a favorable environment for bone remodeling.

Several scientific studies support the development of combined coatings with both antibacterial and osteointegrative properties for orthopedic applications, with a peculiar focus on spinal application [76,77]. The critical challenge of this strategy lies in balancing the different elements, especially of the antibacterial component. If not properly controlled, their toxicity can pose significant issues, particularly at the nanoscale. *In vitro* results seem to suggest the management of silver toxicity through the deposition technique and bone apatite elements that creates a uniform coating capable of gradually releasing silver ions without damaging cellular metabolism.

From a translational perspective, silver coatings represent one of the most extensively investigated strategies, which is crucial for their clinical translation. Nevertheless, other inorganic- and organic-based antibacterial strategies have also been explored. Copper and zinc coatings were shown to exhibit broad-spectrum antimicrobial activity through mechanisms similar to silver, including disruption of bacterial membranes and generation of reactive oxygen species [34,39,48]. However, their ion release profiles are often less controllable, potentially limiting efficacy or increasing cytotoxicity [78]. Antibiotic-loaded coatings can provide targeted bacterial inhibition, but their effectiveness can be compromised by multidrug-resistant strains [79]. Moreover, antibiotic-based coatings are not ideal for infection-prevention purposes because the potential bacterial pathogen is unknown, and organic molecules typically show short release times. In contrast, we show that silver, particularly in nanostructured form, offers antimicrobial action against both gram-positive and gram-negative bacteria, including methicillin-resistant *Staphylococcus aureus*, while allowing modulation of ion release to minimize cytotoxicity. Combining silver with bone apatite further enhances biocompatibility and osteointegration, providing a dual function of antibacterial activity and support of bone regeneration that is challenging to achieve with other metals or antibiotic-based coatings. This combination thus represents a promising approach to develop safe, effective, and multifunctional implant surfaces.

3.5. *In vivo studies*

3.5.1. *In vivo assessment of histocompatibility and osteointegrative properties of nanostructured coatings*

Although the *in vitro* data on these nanostructured coating are stimulating, the information gathered from these studies still requires a higher level of complexity to demonstrate how the combination of 3D porous and rough structure and nano bone apatite coating, which promote bone growth and regeneration, mitigates the potential negative effect of silver. To achieve this, an *in vivo* histocompatibility study was performed.

All animals involved in the histocompatibility *in vivo* study tolerated the implant surgery well, and no local or systemic complications occurred during or after surgery. At the end of the selected experimental time (12 weeks), macroscopic evaluation of the implanted bone segments showed no hematoma, edema/swelling, infection, peri-articular reactions, or any signs related to the implantation of the coated or uncoated materials. Fig. 13**A and** 13**C**, presents a panoramic view of the histological appearance of the CTR substrate and of Ag-Bone coating . No fibrous or connective tissue formation was detected around the nanostructured coating or the surface of the uncoated control material. Direct connection and osteointegration with the host bone were observed, as depicted in Fig. 13**B and** 13**D**, which shows a high magnification detail of material substrates surface. The porous structure and rough surface of the substrate are clearly recognizable. The bone tissue is in direct contact with the coatings, primarily following the rough profiles of the substrate, without the interposition of fibrous tissue.

No adverse inflammatory reactions were found; the cellular population present around the Ag-Bone coating (Fig. 13**D**) resembled bone marrow, whit no accumulations of polymorphonuclear cells (indicative of an acute reaction) or cells associated to a foreign body reaction (giant cells). The coating's ability to stimulate bone tissue regeneration is further evidenced by the fluorescent bands of deposition acquired after tetracycline marking. Presence of double, distinct bands well separated on the surface of the bone trabecula grown were detected in contact with the coating suggesting an active process of deposition and subsequent mineralization, which allowed the incorporation of fluorochrome at the mineralization front.

Finally, histomorphometric data (Table 4) confirmed the qualitative evaluations reported so far: BIC (bone-to-implant contact) data are significantly higher for the Ag-Bone coating compared to the control material, consistently with the lower release of silver and the release of osseointegration-promoting ions, such as *Ca*, measured by ICP.

Despite the presence of silver in the coating, the osteointegration process was higher in comparison to rough porous titanium, which suggests a positive effect of nanostructuring, which dominates over the possible detrimental effect of silver. The dynamic histomorphometry results were not statistically significant, even if slightly higher values for the coating were obtained for both MAR (mineral apposition rate) and BFR (bone formation rate), suggesting that the overall approach based on porosity, nanostructured Ag-Bone coatings and deposition technique, effectively stimulates bone tissue regeneration processes without triggering adverse inflammatory or fibrous reactions.

3.5.2. *Antibacterial efficacy in vivo*

The developed rough porous substrate, when clearly associated with Ag-Bone nanocoating, clearly demonstrate its ability to support and enhance the bone regeneration process, providing the necessary mechanical and structural properties necessary to sustain the load. It also offers an increased growth surface for bone tissue due to the combination of features at the microscale achieved through 3D printing and the nanostructure of the coating. However, the multiscale features increased surface area could also promote bacterial adhesion and growth [80]. In the adopted *in vivo* experimental set-up, this effectiveness was evaluated by replicating condition of device contamination with a "low" bacterial load as per literature data [81] since the aim of these coatings is to prevent the raise of infection and not to cure an existing one. The porous coated and uncoated substrate were immersed in a bacterial suspension for a few minutes prior to implantation, as an alternative to direct bacterial inoculation into bone tissue before device implantation [82].

All animals involved in the antibacterial efficacy study tolerated the implant surgery well, with no local or systemic complications observed during or after the procedure. Results from aerobic and anaerobic blood culture did not reveal the systemic presence of MRSA after 7 days, indicating that infection spread was prevented. Although microbiological data confirmed a local presence of MRSA, none of the animals exhibited clinical signs of local or systemic infection. Analysis of the retrieved substrate samples revealed that 4 out of 5 rabbits showed the presence of bacteria both with the CTR substrates and with Ag-Bone

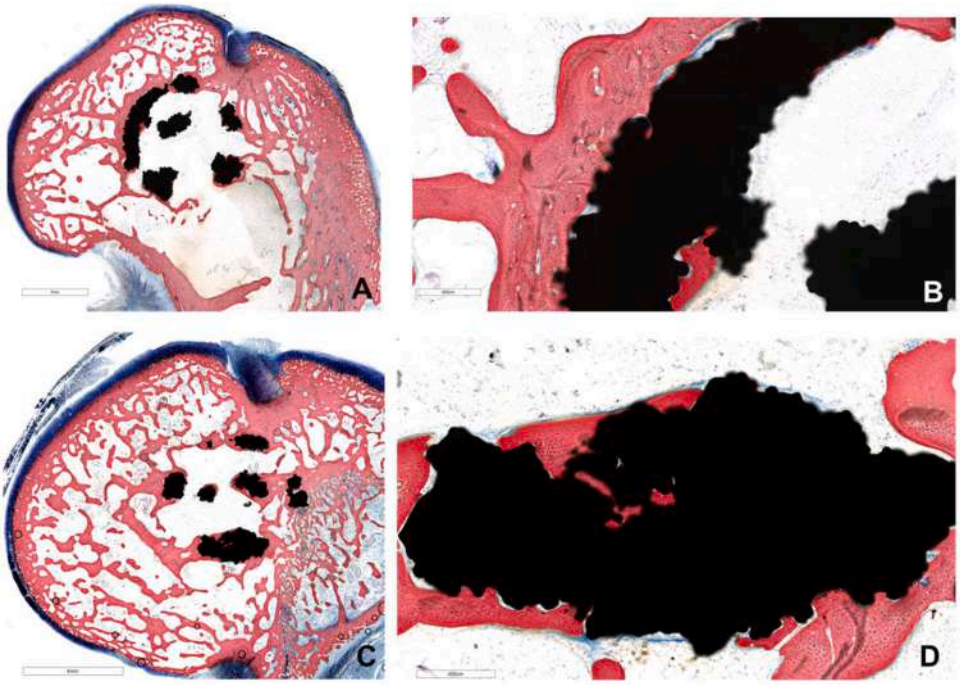

Fig. 13. Figure A and C showed a panoramic view of the of the femoral condyles trabecular component in which the porous CTR (A) and coated substrate (C) has been implanted according to a longitudinal view (Toluidine blue staining counterstained with Van Gieson-Picrofuchsin; acquisition with AperioScanscope CS System, Aperio Technologies, Vista, *CA* – USA at 0.6X magnification; scale bar: 4 mm). Higher magnification reported in Figure B and D show the direct contact between CTR substrate and Ag-Bone coatings and trabecular bone tissue (Toluidine blue staining counterstained with Van Gieson-Picrofuchsin; acquisition with AperioScanscope CS System, Aperio Technologies, Vista, *CA* – USA at 6X magnification; scale bar: 400 μm).

Table 4
Histomorphometric results for Bone to Implant contact (BIC, %), Mineral Apposition Rate (MAR, μm^2/day) and Bone Formation Rate (BFR, $\mu m^3/\mu m^2$/day) parameters, measured for Ag-Bone and Ti-substrate at 12 weeks. Results are reported as Mean ± SD at a significance level of $p < 0.05$ ($^*p < 0.05$).

	BIC (%)	MAR (μm^2/day)	BFR ($\mu m^3/\mu m^2$/day)
Ag-Bone	**32.05 ± 1.3***	**1.12 ± 0.05**	**0.67 ± 0.11**
Ti-substrate	**26.48 ± 1.9**	**0.92 ± 0.08**	**0.60 ± 0.05**

coated substrates, while in the case of pure Ag coating, 2 out of 5 rabbits showed the presence of bacteria 7 days after the MRSA device contamination (Fig. 14**A**). Ag and Ag-Bone coatings had significant efficacy *in vivo* compared to the control. In particular, Ag coating showed the highest inhibition activity of MRSA colonizing the substrate.

Counting the number of MRSA cells in the hemicondyle also confirmed that both coatings have significant activity compared to the control after 7 days of infection (Fig. 14**B**). Indeed, 3 out of 5 animals implanted with Ag showed bacterial cells number below the limit of detection after 7 days, presumably indicating no infection in these rabbits. This indicates that silver is released, and effective, also at a distance from the substrate. This might be due to the uniformity of deposition of the coatings that covers all the areas of the scaffolds. The activity of Ag-Bone was also significant in the hemicondyle although to a lesser extent than the activity of Ag. The reduced antibacterial efficacy of the Ag-Bone coating may be attributed to the lower amount of silver deposited on the alloy surface compared to Ag samples. Additionally, while the bone apatite component is known to enhance

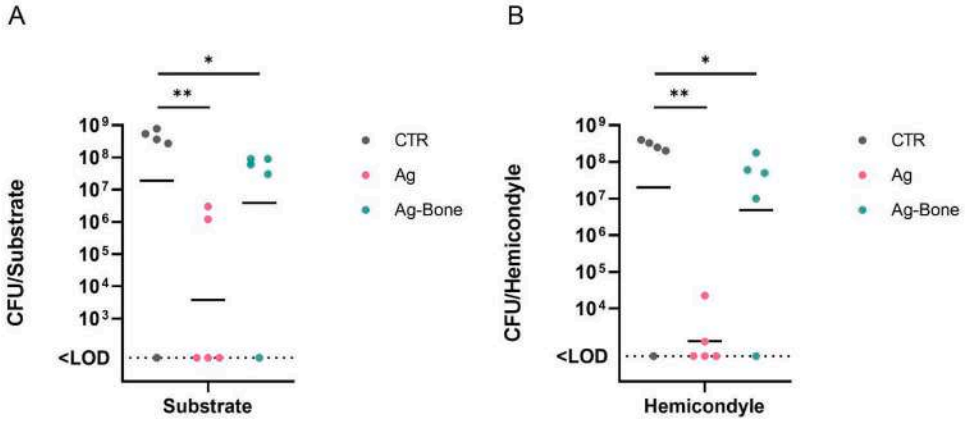

Fig. 14. Bees plot of *in vivo* tests: *S. aureus* USA 300 bacterial contamination on the uncoated (CTR, *i.e.*, control) and coated (Ag and Ag-Bone) substrates (A) implanted in rabbit femur and on hemicondyle surrounding the different prostheses (B) after 7 days. For each group of samples, the solid line indicates the geometric mean. Substrate: CTR *vs* Ag $p = 0.0071$; CTR *vs* Ag-Bone $p = 0.0177$. Hemicondyle: CTR *vs* Ag $p = 0.0046$; CTR *vs* Ag-Bone $p = 0.0271$.

osteointegration, it may also attenuate the antimicrobial activity of silver by acting as a substrate that potentially supports bacterial survival. In both cases, instead, the fact that a similar inhibition is found in the prosthesis (substrate) and the surrounding tissue (hemicondyle) confirms that the deposition reached the deeper areas of the coatings.

Histological images corroborated microbiological data (Fig. 15). Significant bacterial colonization was observed within the bone marrow cavity in animals implanted with CTR substrates (Fig. 15**B)** eliciting an acute inflammation reaction characterized by a prominent presence of polymorphonuclear neutrophils, fibrovascular granulation tissue, and fibrin accumulation. These elements were also present in animals with combined Ag-Bone coatings (Fig. 15**C**), albeit to a lesser extent and confined mainly at the interface between the substrate and bone, with fewer neutrophils. Ag implants exhibited an even milder histological picture, showing fibrovascular tissue reaction and a mild acute response, which aligns with the microbiological data obtained from the bone tissue (Fig. 15**D**). The histological findings were corroborated by the results of the Smeltzer score (**Ag**: 2.0 ± 0.5; **Ag-Bone**: 3.5 ± 0.9; **Ti-substrate (CTR)**: 5.0 ± 0.8) . Although no statistically significant differences were observed among the three materials for the score results, the values obtained for the Ag group suggest a less pronounced inflammatory response compared to that observed with Ti-substrate. Consistent with the microbiological findings, the presence of silver in the Ag-Bone coating also appears to reducing the inflammatory response, albeit to a lesser extent than Ag coating.

Although the antibacterial efficacy of the Ag-Bone combined coating is lower compared to Ag coating, it is still significant compared to the control experiments. The results of the combined coating are extremely important because they integrate several established strategies for the first time creating a device that is: i) safe, ii) mechanically competent yet porous and rough, iii) capable of supporting and promoting bone regeneration both *in vitro* and *in vivo*, and iv) able to exert antibacterial action. Regarding the latter point, some considerations can be made to contextualize the microbiological results. We chose to work with a pathogen - Methicillin-resistant Staphylococcus aureus (MRSA) USA300 placing us in the most challenging conditions. Methicillin-Resistant *Staphylococcus aureus* USA 300 is one of the most threatening strains both in community-associated and hospital-acquired infections, causing severe outcomes when colonizing skin and soft tissues [57,83]. USA300 is characterized by high virulence facilitating its transmission, fast diversification, and acquisition of genetic elements, which drives its evolution and the emergence of new multidrug-resistant lineages [52]. Therefore, our coatings represent promising alternative solutions to drug administration as a prevention strategy against the spreading of USA 300. Interestingly, the efficacy of Ag Bone coatings, is significantly higher than that showed by commercial coatings on the market.

In addition, no pre- or post-operative antibiotic prophylaxis was administered to the animals of the antibacterial efficacy study, to verify the performance of the coatings. Furthermore, in the combined coating, the concentration of silver is naturally lower than in the pure silver coating. The established safety profile of the pure silver coating enables us to consider increasing the silver content in the Ag-Bone coating. This enhancement aims to improve its antibacterial efficacy while preserving its osteoconductive properties.

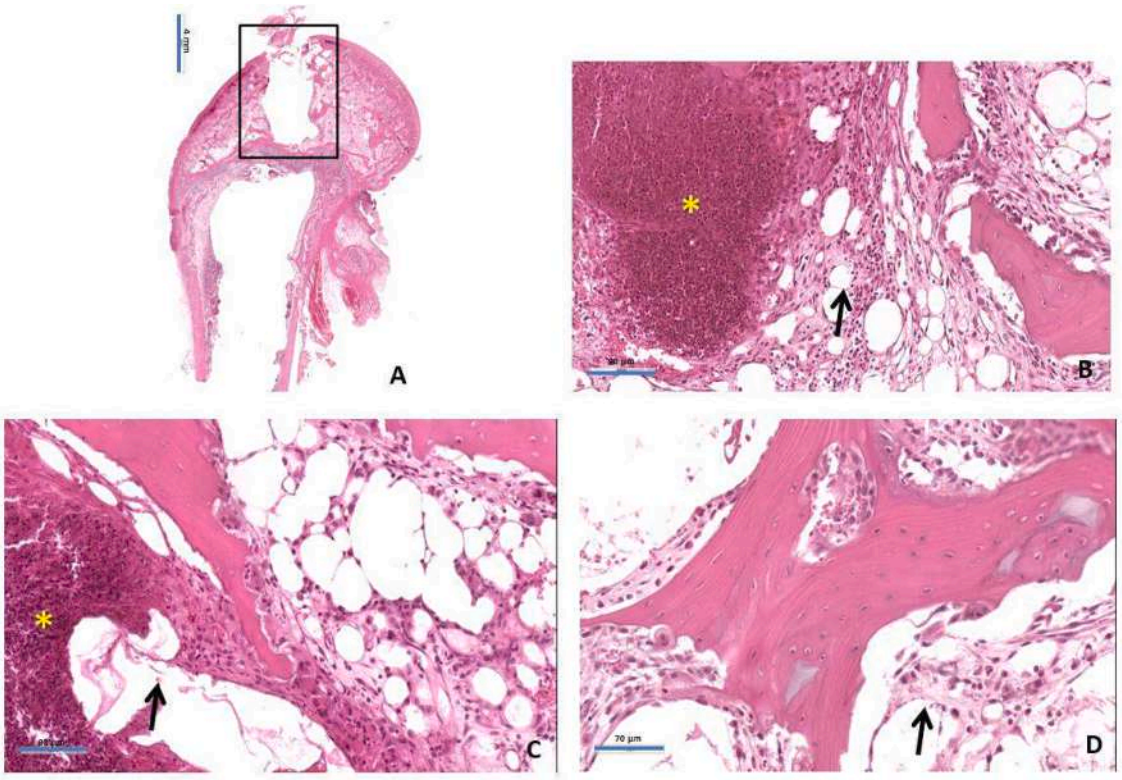

Fig. 15. The top left image (**A**) shows a representative low-magnification view of the distal femoral condyle in a longitudinal cutting plane in which the black box identifies the substrate implantation area (staining Hematoxylin/Eosin. Histological sample was acquired with AperioScanscope AT2 System, Aperio Technologies, Vista, *CA* – USA scale bar: 4 mm, magnification 0.5X). Representative higher magnification details of each implant type are shown in **Figure B** which refers to uncoated substrate (CTR group), **Figure C** refers to Ag-Bone coating group while **Figure D** represents Ag-IJD coating group. All images have been captured at the interface between the coated/uncoated substrate and bone tissue and in which of them, the yellow asterisk (*) has been placed in the areas characterized by an acute inflammatory reaction consisting of neutrophils and granulation tissue (black arrows) in response to the bacterial presence (staining Hematoxylin/Eosin. Histological sample was acquired with AperioScanscope AT2 System, Aperio Technologies, Vista, *CA* – USA (B) scale bar: 90 µm, magnification 23X; (C) scale bar: 80 µm, magnification 25X; (D) scale bar: 70 µm, magnification 30X).

4. Conclusions

Advancements in personalized medicine through additive manufacturing now encompass various medical fields, with orthopedics notably leveraging its numerous benefits. Spine reconstruction surgery has emerged as a significant beneficiary of this approach. This study introduces a groundbreaking approach to create a custom 3D-printed vertebral device designed to replace vertebral bodies affected by tumors or traumatic events. This device is specifically engineered to prevent infection and promote rapid and effective bone regeneration. New antibacterial silver-based films were proposed and validated *in vitro* and *in vivo* to achieve these goals. For the first time, a composite target was developed to deposit silver and bone apatite coatings using ionized jet deposition. Overall, the results demonstrate the applicability of this approach to complex devices for challenging clinical situations. The ability to coat complex scaffolds, including their innermost porosities, could significantly enhance their performance. In detail results show that films maintain the stoichiometry of the target and are nanostructured. Upon optimization of the deposition procedure, shadowing can be mitigated and the whole external and internal surface of a real-scale porous prosthesis can be coated. *In vitro*, the coatings show high efficacy against two *Staphylococcus aureus* (ATCC 6538P and methicillin-resistant USA 300) strains and one *E. coli* (ATCC 8739) strain, as well as high biocompatibility. *In vivo* studies have demonstrated osteointegration for Ag-Bone and antibacterial properties of both manufactured films. Future research will also entail the study of mechanical behavior and stability of the coatings in biomechanically relevant models, simulating insertion of the prostheses in real bone and different cyclic loading condition. The duration of the antibacterial action of the developed coatings is considered satisfactory for addressing primary infection, which was the aim of the paper, however, a long-term evaluation of the durability and efficacy of the coatings at longer timepoints will be carried out to study possible application for addressing late infection. Finally, clinical studies will be necessary to permit bench to bedside translation.

Authorization

In vivo studies were performed in accordance with the Italian Law on animal experimentation, within the framework of projects approved by the Ethics Committee and the Animal Welfare Board of the Rizzoli Orthopaedic Institute and the Ministry of Health, as required by the current Legislative Decree (No. 26/2014), with authorizations **No. 44/2016-PR** for the local effect after implant in bone tissue (histocompatibility study) and authorizations **No. 106/2022-PR** for the antibacterial efficacy study. The *in vivo* protocols were developed in accordance with the PREPARE guidelines (Planning Research and Experimental Procedures an Animals: Recommendations for Excellence) and to further improve the quality of the studies, the *in vivo* research methodology was reported in the manuscript according to criteria set in the Animal in Research: Reporting *in Vivo* Experiments (ARRIVE 2.0) guidelines.

Availability of data and materials

All data supporting the conclusions of this article will be made available by the authors upon reasonable request and without restrictions.

Fundings

This study was performed within the Project founded by National Funding Organizations (Ministero della Salute – IMH) under the frame of EuroNanoMed III Project “Next generation antibacterial nanostructured osseointegrated customized vertebral replacement – NANOVERTEBRA” Joint Transnational call for proposals (JTC 2018).

CRediT authorship contribution statement

Gabriela Graziani: Writing – original draft, Methodology, Investigation, Formal analysis, Conceptualization. **Daniele Ghezzi:** Writing – original draft, Methodology, Investigation, Formal analysis, Conceptualization. **Maria Sartori:** Writing – original draft, Methodology, Investigation, Formal analysis, Conceptualization. **Lucia Martini:** Writing – review & editing, Visualization, Validation, Methodology, Investigation. **Enrico Sassoni:** Writing – original draft, Methodology, Investigation, Formal analysis. **Melania Maglio:** Writing – original draft, Methodology, Investigation, Formal analysis. **Gianluca Giavaresi:** Writing – review & editing, Validation, Supervision, Investigation. **Martina Cappelletti:** Writing – review & editing, Validation, Supervision, Investigation. **Fabio Nudelman:** Formal analysis, Investigation, Methodology, Writing – review & editing. **Marco Boi:** Methodology, Investigation, Formal analysis. **Matteo Montesissa:** Methodology, Investigation, Formal analysis. **Nicola Baldini:** Writing – review & editing, Validation, Supervision. **Fraser Laidlaw:** Formal analysis, Writing – review & editing. **Donato Monopoli:** Writing – review & editing, Methodology, Investigation, Formal analysis. **Giuseppe Tedesco:** Writing – original draft, Methodology, Investigation. **Alessandro Gasbarrini:** Writing – review & editing, Validation, Supervision. **Milena Fini:** Writing – review & editing, Validation, Supervision, Project administration, Funding acquisition, Data curation, Conceptualization.

Declaration of competing interest

The authors declare that they have no known competing financial interests or personal relationships that could have appeared to influence the work reported in this paper.

Acknowledgments

FIB-SEM was performed at the facility at the University of Edinburgh (EPSRC grant No. EP/P030564/1). The Authors would like to thank all the staff involved in the housing, care, and welfare management of the animals involved in this study.

Supplementary materials

Supplementary material associated with this article can be found, in the online version, at doi:10.1016/j.apmt.2025.103062.

Data availability

Data will be made available on request.

References

[1] S. Boriani, A. Gasbarrini, S. Bandiera, R. Ghermandi, R. Lador R, Predictors for surgical complications of en bloc resections in the spine: review of 220 cases treated by the same team, Eur. Spine J. 25 (12) (2016) 3932–3941, https://doi.org/10.1007/s00586-016-4463-y.
[2] S. Boriani, S. Bandiera, S. Colangeli, R. Ghermandi, A. Gasbarrini, En bloc resection of primary tumors of the thoracic spine: indications, planning, morbidity, Neurol. Res. 36 (6) (2014) 566–576, https://doi.org/10.1179/1743132814Y.0000000369.
[3] G.B. Brodano, L. Amendola, K. Martikos, C. Bettuzzi, L. Boriani, A. Gasbarrini, S. Bandiera, S. Terzi, T. Greggi, S. Boriani, Vertebroplasty: benefits are more than risks in selected and evidence-based informed patients. A retrospective study of 59 cases, Eur. Spine J. 20 (8) (2011) 1265–1271, https://doi.org/10.1007/s00586-011-1705-x.
[4] J. De Santo, J.S. Ross, Spine infection/inflammation, Radiol. Clin. North Am. 49 (1) (2011) 105–127, https://doi.org/10.1016/j.rcl.2010.07.018. PMID21111132.
[5] R.M. Duarte, A.R. Vaccaro, Spinal infection: state of the art and management algorithm, Eur. Spine J. 22 (12) (2013) 2787–2799, https://doi.org/10.1007/s00586-013-2850-1.
[6] C.W. Palmer, C.I. Jones, D.K. Park, Postoperative infection of the spine, Sem. Spine Surg. 28 (2016) 134–142, https://doi.org/10.1053/j.semss.2015.07.002.

[7] J.E. Bible, W.F. Donaldson, Postoperative spine infection: prevention and treatment, Oper. Tech. Orthop. 26 (2016) 40–44, https://doi.org/10.1053/j.oto.2015.12.002.

[8] M. Freire-Archer, M. Sarraj, A. Koziarz, P. Thornley, F. Alshaalan, H. Alnemari, E. Kachur, M. Bhandari, C. Oitment, Incidence and recurrence of deep spine surgical site infections: a systematic review and meta-analysis, Spine 48 (16) (2023) E269–E285, https://doi.org/10.1097/BRS.0000000000004713.

[9] X. Wang, Y. Lin, W. Yao, A. Zhang, L. Gao, F. Feng, Surgical site infection in spinal surgery: a bibliometric analysis, J. Orthop. Surg. Res. 18 (1) (2023) 337, https://doi.org/10.1186/s13018-023-03813-6.

[10] W.R. Fordham, S. Redmond, A. Westerland, E.G. Cortes, C. Walker, et al., Silver as a bactericidal coating for biomedical implants, Surf. Coat. Technol. 253 (2014) 52–57, https://doi.org/10.1016/j.surfcoat.2014.05.013.

[11] V. Alt, Antimicrobial coated implants in trauma and orthopaedics-A clinical review and risk-benefit analysis, Injury 48 (3) (2017) 599–607, https://doi.org/10.1016/j.injury.2016.12.011.

[12] J. Raphel, M. Holodniy, S.B. Goodman, S.C. Heilshorn, Multifunctional coatings to simultaneously promote osseointegration and prevent infection of orthopaedic implants, Biomaterials 84 (2016) 301–314, https://doi.org/10.1016/j.biomaterials.2016.01.016.

[13] S. Ciuca, M. Badea, E. Pozna, I. Pana, A. Kiss, L. Floroian, A. Semenescu, C. M. Cotrut, M. Moga, A. Vladescu, Evaluation of Ag containing hydroxyapatite coatings to the Candida albicans infection, J. Microbiol. Methods 125 (2016) 12–18, https://doi.org/10.1016/j.mimet.2016.03.016.

[14] M. Badea, M. Braic, A. Kiss, M. Moga, E. Pozna, I. Pana, A. Vladescu, Influence of Ag content on the antibacterial properties of SiC doped hydroxyapatite coatings, Ceram. Int. 42 (1, Part B) (2016) 1801–1811, https://doi.org/10.1016/j.ceramint.2015.09.143.

[15] D. Giacomini, P. Torricelli, G.A. Gentilomi, E. Boanini, M. Gazzano, F. Bonvicini, E. Benetti, R. Soldati, G. Martelli, K. Rubini, A. Bigi, Monocyclic β-lactams loaded on hydroxyapatite: new biomaterials with enhanced antibacterial activity against resistant strains, Sci. Rep. 7 (1) (2017) 2712, https://doi.org/10.1038/s41598-017-02943-2.

[16] L. Forte, P. Torricelli, F. Bonvicini, E. Boanini, G.A. Gentilomi, G. Lusvardi, E. Della Bella, M. Fini, E. Vecchio Nepita, A. Bigi, Biomimetic fabrication of antibacterial calcium phosphates mediated by polydopamine, J. Inorg. Biochem. 178 (2018) 43–53, https://doi.org/10.1016/j.jinorgbio.2017.10.004.

[17] A. Rodriguez-Palomo, D. Monopoli, H. Afonso, I. Izquierdo-Barba, M. Vallet-Regí, Surface zwitterionization of customized 3D Ti6Al4V scaffolds: a promising alternative to eradicate bone infection, J. Mater. Chem. B 4 (24) (2016) 4356–4365, https://doi.org/10.1039/c6tb00675b.

[18] G. Graziani, K. Barbaro, I.V. Fadeeva, D. Ghezzi, M. Fosca, E. Sassoni, G. Vadalà, M. Cappelletti, F. Valle, N. Baldini, J.V. Rau, Ionized jet deposition of antimicrobial and stem cell friendly silver-substituted tricalcium phosphate nanocoatings on titanium alloy, Bioact. Mater. 6 (8) (2021) 2629–2642, https://doi.org/10.1016/j.bioactmat.2020.12.019.

[19] B. Wilcox, R.J. Mobbs, A.M. Wu, K. Phan, Systematic review of 3D printing in spinal surgery: the current state of play, J. Spine Surg. 3 (3) (2017) 433–443, https://doi.org/10.21037/jss.2017.09.01.

[20] R. Costanzo, G. Ferini, L. Brunasso, L. Bonosi, M. Porzio, U.E. Benigno, S. Musso, R. M. Gerardi, et al., The role of 3D-printed custom-made vertebral body implants in the treatment of spinal tumors: a systematic review, Life 12 (4) (2022) 489, https://doi.org/10.3390/life12040489.

[21] E.D. Sheha, S.D. Gandhi, M.W. Colman, 3D printing in spine surgery, Ann. Transl. Med. 7 (Suppl 5) (2019) S164, https://doi.org/10.21037/atm.2019.08.88.

[22] Y. Wu, J. Liu, L. Kang, J. Tian, X. Zhang, J. Hu, Y. Huang, F. Liu, H. Wang, Z. Wu, An overview of 3D printed metal implants in orthopedic applications: present and future perspectives, Heliyon 9 (7) (2023) e17718, https://doi.org/10.1016/j.heliyon.2023.e17718.

[23] H. Zhou, S. Liu, Z. Li, X. Liu, L. Dang, Y. Li, Z. Li, P. Hu, B. Wang, F. Wei, Z. Liu, 3D-printed vertebral body for anterior spinal reconstruction in patients with thoracolumbar spinal tumors, J. Neurosurg. Spine 37 (2) (2022) 274–282, https://doi.org/10.3171/2022.1.SPINE21900.

[24] M. Girolami, S. Boriani, S. Bandiera, G. Barbanti-Bródano, R. Ghermandi, S. Terzi, G. Tedesco, G. Evangelisti, V. Pipola, A. Gasbarrini, Biomimetic 3D-printed custom-made prosthesis for anterior column reconstruction in the thoracolumbar spine: a tailored option following en bloc resection for spinal tumors: preliminary results on a case-series of 13 patients, Eur. Spine J. 27 (12) (2018) 3073–3083, https://doi.org/10.1007/s00586-018-5708-8.

[25] M. Girolami, M. Sartori, D. Monopoli-Forleo, R. Ghermandi, G. Tedesco, G. Evangelisti, V. Pipola, E. Pesce, L. Falzetti, M. Fini, A. Gasbarrini, Histological examination of a retrieved custom-made 3D-printed titanium vertebra: do the fine details obtained by additive manufacturing really promote osteointegration? Eur. Spine J. 30 (10) (2021) 2775–2781, https://doi.org/10.1007/s00586-021-06926-w.

[26] N.J. Pertsch, O.P. Leary, J.Q. Camara-Quintana, D.D. Liu, T. Niu, A.S. Woo, T. T. Ng, A.A. Oyelese, J.S. Fridley, Z.L. Gokaslan, A modern multidisciplinary approach to a large cervicothoracic chordoma using staged en bloc resection with intraoperative image-guided navigation and 3D-printed modeling: illustrative case, J. Neurosurg. Case Lessons 1 (6) (2021) CASE2023, https://doi.org/10.3171/CASE2023.

[27] Z. Sun, M. Yin, Y. Sun, M. Cheng, M. Fang, W. Huang, J. Ma, W. Yan, Customized multilevel 3D printing implant for reconstructing spine tumor: a retrospective case series study in a single center, Orthop. Surg. 14 (9) (2022) 2016–2022, https://doi.org/10.1111/os.13357.

[28] M. Sartori, G. Graziani, E. Sassoni, S. Pagani, M. Boi, M.C. Maltarello, N. Baldini, M. Fini, Nanostructure and biomimetics orchestrate mesenchymal stromal cell differentiation: an in vitro bioactivity study on new coatings for orthopedic applications, Mater. Sci. Eng. C Mater. Biol. Appl. 123 (2021) 112031, https://doi.org/10.1016/j.msec.2021.112031.

[29] S.V. Dorozhknin, Calcium orthophosphate coatings, films and layers, Prog. Biomater. 1 (1) (2012) 1, https://doi.org/10.1186/2194-0517-1-1.

[30] A.G. Tsantes, D.V. Papadopoulos, G. Vrioni, S. Sioutis, G. Sapkas, A. Benzakour, T. Benzakour, A. Angelini, P. Ruggieri, A.F. Mavrogenis, World association against infection in orthopedics and trauma W A I O T study group on bone and joint infection definitions. spinal infections: an update, Microorganisms 8 (4) (2020) 476, https://doi.org/10.3390/microorganisms8040476.

[31] G.A. Gonzalez, G. Porto, E. Tecce, Y.S. Oghli, J. Miao, M. O'Leary, D.P. Chadid, M. Vo, J. Harrop, Advances in diagnosis and management of atypical spinal infections: a comprehensive review, N Am. Spine Soc. J. 16 (2023) 100282, https://doi.org/10.1016/j.xnsj.2023.100282.

[32] M.K. Kasliwal, L.A. Tan, V.C. Traynelis, Infection with spinal instrumentation: review of pathogenesis, diagnosis, prevention, and management, Surg. Neurol. Int. 4 (Suppl 5) (2013) S392–S403, https://doi.org/10.4103/2152-7806.120783.

[33] J.E. Trapana, J.P. Gjolaj, Infections of the spine, Semin. Spine Surg. 34 (1) (2022) 100922, https://doi.org/10.1016/j.semss.2022.100922.

[34] D. Ghezzi, M. Boi, E. Sassoni, M. Cappelletti, G. Graziani, Customized biofilm device for antibiofilm and antibacterial screening of newly developed nanostructured silver and zinc coatings, J. Biol. Eng. 17 (1) (2023) 18, https://doi.org/10.1186/s13036-023-00326-y.

[35] T. Fischetti, G. Graziani, D. Ghezzi, F. Kaiser, S. Hoelscher-Doht, M. Cappelletti, G. Barbanti-Bròdano, J. Groll, N. Baldini, U. Gbureck, T. Jungst, Combining 3D printing and cryostructuring to tackle infection and spine fusion, Adv. Mater. Technol. 9 (5) (2024) 2301301, https://doi.org/10.1002/admt.202301301.

[36] G. Graziani, D. Ghezzi, F. Nudelman, E. Sassoni, F. Laidlaw, M. Cappelletti, M. Boi, G. Borciani, S. Milita, M. Bianchi, N. Baldini, G. Falini, A natural biogenic fluorapatite as a new biomaterial for orthopedics and dentistry: antibacterial activity of lingula seashell and its use for nanostructured biomimetic coatings, J. Mater. Chem. B 12 (8) (2024) 2083–2098, https://doi.org/10.1039/d3tb02454g.

[37] F. Paladini, M. Pollini, A. Talà, P. Alifano, A. Sannino, Efficacy of silver treated catheters for haemodialysis in preventing bacterial adhesion, J. Mater. Sci. Mater. Med. 23 (8) (2012) 1983–1990, https://doi.org/10.1007/s10856-012-4674-7.

[38] W.R. Fordham, S. Redmond, A. Westerland, E.G. Cortes, C. C.Walker, C.J. Medina, C. F.Waecther, R.F. Ostrume, G.A. Caputo, J.D. Hettinger, R.R. Krchnavek, Silver as a bactericidal coating for biomedical implants, Surf. Coat. Technol. 253 (2014) 52–57.

[39] D. Ghezzi, E. Sassoni, M. Boi, M. Montesissa, N. Baldini, G. Graziani, M. Cappelletti, Antibacterial and antibiofilm activity of nanostructured copper films prepared by ionized jet deposition, Antibiotics 12 (1) (2022) 55, https://doi.org/10.3390/antibiotics12010055.

[40] D. Ghezzi, G. Graziani, M. Cappelletti, I.V. Fadeeva, M. Montesissa, E. Sassoni, G. Borciani, K. Barbaro, M. Boi, N. Baldini, J.V. Rau, New strontium-based coatings show activity against pathogenic bacteria in spine infection, Front. Bioeng. Biotechnol. 12 (2024) 1347811, https://doi.org/10.3389/fbioe.2024.1347811.

[41] R. Bambauer, P. Mestres, R. Schiel, J. Klinkmann, P. Sioshansi, Surface-treated catheters with ion beam-based process evaluation in rats, Artif Organs 21 (9) (1997) 1039–1041, https://doi.org/10.1111/j.1525-1594.1997.tb00520.x.

[42] S. Sério, Advanced nanostructured coatings deposited by magnetron sputtering: innovations, applications, and future prospects, Coatings. 14 (8) (2024) 1041, https://doi.org/10.3390/coatings14081041.

[43] G. Graziani, D. Ghezzi, M. Boi, N. Baldini, E. Sassoni, M. Cappelletti, G. Fedrizzi, M. Maglio, F. Salamanna, M. Tschon, L. Martini, S. Zaffagnini, M. Fini, M. Sartori, Ionized jet deposition of silver nanostructured coatings: assessment of chemico-physical and biological behavior for application in orthopedics, Biomater Adv 159 (2024) 213815, https://doi.org/10.1016/j.bioadv.2024.213815.

[44] M. Jäger, H.P. Jennissen, F. Dittrich, A. Fischer, H.L. Köhling, Antimicrobial and Osseointegration Properties of Nanostructured Titanium Orthopaedic Implants, Materials 10 (119) (2017) 1302, https://doi.org/10.3390/ma10111302.

[45] S. Castiglioni, A. Cazzaniga, L. Locatelli, J.A.M. Maier, Silver nanoparticles in orthopedic applications: new insights on their effects on osteogenic cells, Nanomaterials. 7 (6) (2017) 124, https://doi.org/10.3390/nano7060124.

[46] C.E. Albers, W. Hofstetter, K.A. Siebenrock, R. Landmann, F.M. Klenke, In vitro cytotoxicity of silver nanoparticles on osteoblasts and osteoclasts at antibacterial concentrations, Nanotoxicology 7 (1) (2013) 30–36, https://doi.org/10.3109/17435390.2011.626538.

[47] M. Rai, A. Yadav, A. Gade, Silver nanoparticles as a new generation of antimicrobials, Biotechnol Adv 27 (1) (2009) 76–83, https://doi.org/10.1016/j.biotechadv.2008.09.002.

[48] J.A. Lemire, J.J. Harrison, R.J. Turner, Antimicrobial activity of metals: mechanisms, molecular targets and applications, Nat. Rev. Microbiol. 11 (6) (2013) 371–384, https://doi.org/10.1038/nrmicro3028.

[49] J. Hou, L. Zhao, H. Tang, X. He, G. Ye, F. Shi, M. Kang, H. Chen, Y. Li, Silver nanoparticles induced oxidative stress and mitochondrial injuries mediated autophagy in HC11 Cells through Akt/AMPK/mTOR pathway, Biol. Trace Elem. Res. 199 (3) (2021) 1062–1073, https://doi.org/10.1007/s12011-020-02212-w.

[50] M. Montesissa, E. Sassoni, M. Boi, G. Borciani, E. Boanini, G. Graziani, Synthetic or natural (bio-based) hydroxyapatite? A systematic comparison between biomimetic nanostructured coatings produced by ionized jet deposition, Nanomaterials 14 (16) (2024) 1332, https://doi.org/10.3390/nano14161332.

[51] M. Bianchi, A. Pisciotta, L. Bertoni, M. Berni, A. Gambardella, A. Visani, A. Russo, A. de Pol, G. Carnevale, Osteogenic differentiation of hDPSCs on biogenic bone apatite thin films, Stem Cell Int. 579283 (2017) 1–10, https://doi.org/10.1155/2017/3579283.
[52] T.D. Read, R.A. Petit, Z. Yin, et al., USA300 Staphylococcus aureus persists on multiple body sites following an infection, BMC Microbiol. 18 (2018) 206, https://doi.org/10.1186/s12866-018-1336-z.
[53] A.M. Crovace, L. Lacitignola, D.M. Forleo, F. Staffieri, E. Francioso, A. Di Meo, J. Becerra, A. Crovace, L. Santos-Ruiz, 3D biomimetic porous titanium (Ti6Al4V ELI) scaffolds for large bone critical defect reconstruction: an experimental study in sheep, Animals 10 (8) (2020) 1389, https://doi.org/10.3390/ani10081389.
[54] G. Graziani, M. Berni, A. Gambardella, M. De Carolis, M.C. Maltarello, M. Boi, G. Carnevale, M. Bianchi, Fabrication and characterization of biomimetic hydroxyapatite thin films for bone implants by direct ablation of a biogenic source, Mater. Sci. Eng. C Mater. Biol. Appl. 99 (2019) 53–862, https://doi.org/10.1016/j.msec.2019.02.033.
[55] A. Liguori, C. Gualandi, M.L. Focarete, F. Biscarini, M. Bianchi, The pulsed electron deposition technique for biomedical applications: a review, Coatings 10 (1) (2020) 16, https://doi.org/10.3390/coatings10010016.
[56] S. Dyzenhaus, M.J. Sullivan, B. Alburquerque, et al., MRSA lineage USA300 isolated from bloodstream infections exhibit altered virulence regulation, Cell Host Microbe 31 (2) (2023) 228–242.e8, https://doi.org/10.1016/j.chom.2022.12.003, 8.
[57] B.A. Diep, S.R. Gill, R.F. Chang, T.H. Phan, J.H. Chen, M.G. Davidson, F. Lin, J. Lin, H.A. Carleton, E.F. Mongodin, G.F. Sensabaugh, F. Perdreau-Remington, Complete genome sequence of USA300, an epidemic clone of community-acquired meticillin-resistant Staphylococcus aureus, Lancet 367 (9512) (2006) 731–739, https://doi.org/10.1016/S0140-6736(06)68231-7.
[58] A.J. Smith, R.E. Clutton, E. Lilley, K.E.A. Hansen, T. Brattelid, PREPARE: guidelines for planning animal research and testing, Lab. Anim. 52 (2) (2018) 135–141, https://doi.org/10.1177/0023677217724823.
[59] A. Scarano, A.G.A. Khater, S.A. Gehrke, F. Inchingolo, S.R. Tari, Animal models for investigating osseointegration: an overview of implant research over the last three decades, J. Funct. Biomater. 15 (2024) 83.
[60] A.I. Pearce, R.G. Richards, S. Milz, E. Schneider, S.G. Pearce, Animal models for implant biomaterial research in bone: a review, Eur. Cell Mater. 13 (2007 Mar 2) 1–10.
[61] N. Percie du Sert, A. Ahluwalia, S. Alam, M.T. Avey, M. Baker, W.J. Browne, et al., Reporting animal research: explanation and elaboration for the ARRIVE guidelines 2.0, PLoS Biol. 18 (7) (2020) e3000411, https://doi.org/10.1371/journal.pbio.3000411.
[62] D.W. Dempster, J.E. Compston, M.K. Drezner, F.H. Glorieux, J.A. Kanis, H. Malluche, P.J. Meunier, S.M. Ott, R.R. Recker, A.M. Parfitt, Standardized nomenclature, symbols, and units for bone histomorphometry: a 2012 update of the report of the ASBMR Histomorphometry Nomenclature Committee, J. Bone Miner. Res. 28 (1) (2013) 2–17, https://doi.org/10.1002/jbmr.1805.
[63] M.S. Smeltzer, J.R. Thomas, S.G. Hickmon, R.A. Skinner, C.L. Nelson, D. Griffith, T. R. Parr Jr, Evans Characterization of a rabbit model of staphylococcal osteomyelitis, Orthop. Res. 15 (3) (1997) 414–421. May.
[64] G. Bjerkan, E. Witsø, K. Bergh, Sonication is superior to scraping for retrieval of bacteria in biofilm on titanium and steel surfaces in vitro, Acta Orthop 80 (2) (2009) 245–250, https://doi.org/10.3109/17453670902947457.
[65] K. Trampuz, M.J. Jacobson, A.D. Hanssen, K.K. Unni, D.R. Osmon, J.N. Mandrekar, F.R. Cockerill, J.M. Steckelberg, J.F. Greenleaf, R. Patel, Sonication of removed hip and knee prostheses for diagnosis of infection, N. Engl. J. Med. 357 (7) (2007) 654–663, https://doi.org/10.1056/NEJMoa061588, 16.
[66] G. Di Pompo, A. Liguori, M. Carlini, et al., Electrospun fibers coated with nanostructured biomimetic hydroxyapatite: a new platform for regeneration at the bone interfaces, Biomater. Adv. 144 (2023) 213231, https://doi.org/10.1016/j.bioadv.2022.213231.
[67] Q.L. Feng, J. Wu, G.Q. Chen, F.Z. Cui, T.N. Kim, J.O. Kim, A mechanistic study of the antibacterial effect of silver ions on Escherichia coli and Staphylococcus aureus, J. Biomed. Mater. Res. 52 (4) (2000) 662–668, https://doi.org/10.1002/1097-4636(20001215)52:4<662::aid-jbm10>3.0.co;2-3, 15.
[68] J.V. Loh, S.L. Percival, E.J. Woods, N.J. Williams, C.A. Cochrane, Silver resistance in MRSA isolated from wound and nasal sources in humans and animals, Int. Wound. J. 6 (1) (2009) 32–38, https://doi.org/10.1111/j.1742-481X.2008.00563.x.
[69] J. Hu, G. Song, C. H, et al., Surgical outcomes and risk factors for surgical complications after en bloc resection following reconstruction with 3D-printed artificial vertebral body for thoracolumbar tumors, World J. Surg. Oncol. 21 (1) (2023) 385, https://doi.org/10.1186/s12957-023-03271-8.
[70] Y. Cao, N. Yang, S. Wang, C. Wang, Q. He, Q. Wu, Y. Zheng, The application of 3D-printed auto-stable artificial vertebral body in en bloc resection and reconstruction of thoracolumbar metastases, J. Orthop. Surg. Res. 18 (1) (2023) 638, https://doi.org/10.1186/s13018-023-04135-3.
[71] C.E. Albers, W. Hofstetter, K.A. Siebenrock, R. Landmann, F.M. Klenke, In vitro cytotoxicity of silver nanoparticles on osteoblasts and osteoclasts at antibacterial concentrations, Nanotoxicology 7 (2013) 30–36, https://doi.org/10.3109/17435390.2011.626538.
[72] Y. Wu, X. Shi, J. Wang, Y. Li, J. Wu, D. Jia, Y. Bai, X. Wu, Y. Xu, A surface metal ion-modified 3D-printed Ti-6Al-4V implant with direct and immunoregulatory antibacterial and osteogenic activity, Front. Bioeng. Biotechnol. 11 (2023) 1142264, https://doi.org/10.3389/fbioe.2023.1142264.
[73] A. Strasser, L. O'Connor, V.M. Dixit, Apoptosis signaling, Annu. Rev. Biochem. 69 (2000) 217–245, https://doi.org/10.1146/annurev.biochem.69.1.217.
[74] P. Castrogiovanni, F.M. Trovato, M.A. Szychlinska, H. Nsir, R. Imbesi, G. Musumeci, The importance of physical activity in osteoporosis. From the molecular pathways to the clinical evidence, Histol. Histopathol. 31 (11) (2016) 1183–1194, https://doi.org/10.14670/HH-11-793.
[75] S. Castiglioni, A. Cazzaniga, L. Locatelli, J.A.M. Maier, Silver nanoparticles in orthopedic applications: new insights on their effects on osteogenic cells, Nanomaterials 7 (6) (2017) 124, https://doi.org/10.3390/nano7060124.
[76] X. Lu, Z. Wu, K. Xu, X. Wang, S. Wang, H. Qiu, X. Li, J. Chen, Multifunctional coatings of titanium implants toward promoting osseointegration and preventing infection: recent developments, Front. Bioeng. Biotechnol. 9 (2021) 783816, https://doi.org/10.3389/fbioe.2021.783816.
[77] T. Morimoto, H. Hirata, S. Eto, A. Hashimoto, S. Kii, et al., Development of silver-containing hydroxyapatite-coated antimicrobial implants for orthopaedic and spinal surgery, Medicina) 58 (2022) 519, https://doi.org/10.3390/medicina58040519.
[78] Y. Wu, H. Zhou, Y. Zeng, H. Xie, D. Ma, Z. Wang, H. Liang, Recent advances in copper-doped titanium implants, Materials 15 (7) (2022) 2342, https://doi.org/10.3390/ma15072342, 22.
[79] X. Chen, J. Zhou, Y. Qian, L. Zhao, Antibacterial coatings on orthopedic implants, Mater Today Bio 15 (19) (2023) 100586, https://doi.org/10.1016/j.mtbio.2023.100586.
[80] D. Ghezzi, G. Graziani, M. Cappelletti, I.V. Fadeeva, M. Montesissa, E. Sassoni, G. Borciani, K. Barbaro, M. Boi, N. Baldini, J.V. Rau, New strontium-based coatings show activity against pathogenic bacteria in spine infection, Front. Bioeng. Biotechnol. 12 (2024) 1347811, https://doi.org/10.3389/fbioe.2024.1347811.
[81] M. Bottagisio, C. Coman, A.B. Lovati, Animal models of orthopaedic infections. A review of rabbit models used to induce long bone bacterial infections, J. Med. Microbiol. 68 (4) (2019) 506–537, https://doi.org/10.1099/jmm.0.000952.
[82] M. Fabritius, A.A. Al-Munajjed, C. Freytag, H. Jülke, M. Zehe, T. Lemarchand, J. J. Arts, D. Schumann, V. Alt, K. Sternberg, Antimicrobial silver multilayer coating for prevention of bacterial colonization of orthopedic implants, Materials 13 (6) (2020) 1415, https://doi.org/10.3390/ma13061415.
[83] S. Dyzenhaus, M.J. Sullivan, B. Alburquerque, D. Boff, A. van de Guchte, M. Chung, Y. Fulmer, R. Copin, et al., MRSA lineage USA300 isolated from bloodstream infections exhibit altered virulence regulation, Cell Host Microbe 31 (2) (2023) 228–242.e8, https://doi.org/10.1016/j.chom.2022.12.003.